An impressionist view of V Hydrae

L. Planquart, C. Paladini, A. Jorissen, A. Escorza, E. Pantin, J. Drevon, B. Aringer, F. Baron, A. Chiavassa, P. Cruzalèbes, et al.

A&A, 687, A306 (2024)
https://doi.org/10.1051/0004-6361/202348226

Astronomy & Astrophysics

An impressionist view of V Hydrae

When MATISSE paints asymmetric giant blobs★

L. Planquart[1,2,★★], C. Paladini[2], A. Jorissen[1], A. Escorza[2,3,4], E. Pantin[5], J. Drevon[2,6], B. Aringer[7], F. Baron[8], A. Chiavassa[6], P. Cruzalèbes[6], W. Danchi[9], E. De Beck[10], M. A. T. Groenewegen[11], S. Höfner[12], J. Hron[7], T. Khouri[10], B. Lopez[6], F. Lykou[13], M. Montarges[14], N. Nardetto[6], K. Ohnaka[15], H. Olofsson[10], G. Rau[9], A. Rosales-Guzmán[16], J. Sanchez-Bermudez[16], P. Scicluna[2], L. Siess[1], F. Thévenin[6], S. Van Eck[1], W. H. T. Vlemmings[10], G. Weigelt[17], and M. Wittkowski[18]

(Affiliations can be found after the references)

Received 10 October 2023 / Accepted 1 May 2024

ABSTRACT

Context. Asymptotic giant branch (AGB) stars enrich the interstellar medium through their mass loss. The mechanism(s) shaping the circumstellar environment of mass-losing stars is not clearly understood so far.
Aims. Our purpose is to study the effect of binary companions located within the first 10 stellar radii from the primary AGB star. In this work, we target the mass-losing carbon star V Hydrae (V Hya) and search for signatures of its companion in the dust-forming region of the atmosphere.
Methods. The star was observed in the *L* and *N* bands with the VLTI/MATISSE instrument at low spectral resolution. We reconstructed images of the photosphere and surroundings of V Hya using the two bands and compared our interferometric observables with VLTI/MIDI and VISIR archival data. To constrain the dust properties, we used the 1D radiative transfer code DUSTY to model the spectral energy distribution.
Results. The star is dominated by dust emission in the *L*- and *N*-bands. The MATISSE reconstructed images show asymmetric and elongated structures in both infrared bands. In the *L* band, we detected an elongated shape of approximately 15 mas that likely is of photospheric origin. In the *N* band, we found a 20 mas extension northeast from the star and perpendicular to the *L*-band elongated axis. The position angle and the size of the *N*-band extension match the prediction of the companion position at the MATISSE epoch. By comparing MATISSE *N*-band with MIDI data, we deduce that the elongation axis in the *N*-band has rotated since the previous interferometric measurements 13 yr ago, supporting the idea that the particle enhancement is related to the dusty clump moving along with the companion. The VISIR image confirms the presence of a large-scale dusty circumstellar envelope surrounding V Hya.
Conclusions. The MATISSE images unveil the presence of a dust enhancement at the position of the companion. This opens new doors for further analyses of the binary interaction with an AGB component.

Key words. techniques: interferometric – stars: AGB and post-AGB – stars: carbon – stars: mass-loss – stars: individual: V Hydrae

1. Introduction

During the Asymptotic giant branch (AGB) phase, low- to intermediate-mass stars eject most of their mass through stellar winds ($\dot{M} > 10^{-8}\ M_\odot\ \mathrm{yr}^{-1}$; Höfner & Olofsson 2018), contributing to the dust and chemical enrichment of the Galaxy. When they begin their transition from the AGB to the pre-planetary nebula (pPN) or post-AGB phase, a variety of complex geometries arises. The emergence of asymmetric outflows in these final stages of stellar evolution (multipolar jets, spirals, or discs) is thought to be driven by the interaction of the AGB environment with a binary companion (Jones & Boffin 2017; Decin et al. 2020). However, there are two main limitations in trying to detect binary companions of evolved stars: on one hand, the primary is close and much brighter (a few hundred to a thousand times) than the secondary, limiting direct-imaging detection of the companion. On the other hand, the AGB star often exhibits strong variability related to pulsation, making indirect detection of the companion through radial-velocity difficult as well. Only a few AGB binaries have been detected so far, and very few of them have been studied in depth (e.g. Ramstedt et al. 2014; Kervella et al. 2016; Doan et al. 2020). Direct observations of these systems are nevertheless needed to improve our understanding of the mechanism with which the stellar wind shapes the geometries. The BIN-AGB ESO Large Program (nickname for BINary AGBs, PI Paladini, prog ID: 108.22E9) aims at imaging the first 10 stellar radii of ten different AGB stars with different chemistry and variability classes. Many of the targets, including the target presented here, are suspected binaries, and the main aim is to observe how the presence of a companion affects the onset and morphology of the stellar wind.

V Hydrae (V Hya) is a carbon star that exhibits peculiar properties for an AGB star: a high mass-loss rate ($10^{-5}\ M_\odot\ \mathrm{yr}^{-1}$, Knapp et al. 1997), a mean spectral broadening of 13.5 $\mathrm{km\,s}^{-1}$ with a periodic variation of 9 $\mathrm{km\,s}^{-1}$ (Barnbaum et al. 1995), and a dense equatorial disc combined with a bipolar outflow mapped by the radio emission of CO $J = 2$–1 and $J = 3$–2 (from a 15″ spatial mesh). The latter suggests that the star may be at the transition from the AGB phase to a planetary nebula, and its

★ Based on observations made at the Paranal Observatory under ESO Programmes ID 108.22E9, 096.D-0568, and 079.D-0140(A).
★★ Research fellow, NRS, Belgium.

environment is shaped by a companion (Tsuji et al. 1988; Kahane et al. 1996; Hirano et al. 2004). The distance estimates to V Hya range from 340 pc to 550 pc (Barnbaum et al. 1995; Bergeat et al. 1998) and the measured parallax of 2.31 ± 0.11 mas corresponds to a distance of 434 ± 21 pc (Gaia Collaboration 2021), which is adopted in the current paper[1].

Photometric monitoring in the visual band shows a nearly sinusoidal variation with a period of 530 ± 30 days, typical of Mira-type stars, as well as a periodic dimming event every 17 ± 1 yr. Knapp et al. (1999) interpreted the dimming event as caused by a thick cloud that orbits the star and is connected to the binary companion. Hints of the presence of a companion were also revealed by the detection of forbidden emission lines in the blue part of the optical spectrum (Lloyd Evans 1991) and by an excess of UV flux that Sahai et al. (2008) explained as arising from a hot accretion disc surrounding the companion. An accretion disc resulting from mass transfer in a binary system was also suggested as the origin of the varying high-velocity (up to 120 km s^{-1}) jet seen in the 4.6 μm CO vibration-rotation band (Sahai & Wannier 1988; Sahai et al. 2009) and in optical atomic lines (Lloyd Evans 1991; Planquart et al. 2024). From a long-term radial velocity monitoring combined with proper motion acceleration, Planquart et al. (2024) proposed an orbital solution with an orbital period of 17.5 yr, a low eccentricity, and an inclination angle of 40° between the orbital plane and the plane of sky, leading to a separation of about 11 au. Given the orbital model, the periodic dimming event coincides with the superior conjunction and is explained by a dusty clump that moves with the companion, whereas the blueshifted absorption lines are explained by the presence of a conical high-velocity jet launched at the position of the companion.

Previous imaging studies already demonstrated the complex circumstellar environment around the star at different scales, however, none of them directly identified the companion. Starting from the large spatial scales at the interface with the interstellar medium, ALMA images at an angular resolution of 0.5″ (220 au adopting a distance of 434 pc) by Sahai et al. (2022) revealed concentric rings and bipolar arcs surrounding the star in the sub-millimeter range. HST images taken at six different epochs showed that the system undergoes periodic ejections of so-called bullets in the form of high-velocity collimated material seen in the emission line of [S II] (Sahai et al. 2016).

With the Gemini Planet Imager instrument (GPI), Sahai et al. (2019) imaged the polarized (scattered) light of an extended central dusty disc (radius ∼0.5″) in the near-infrared (Y band). The dusty environment was imaged in the thermal infrared (N band) with the mid-infrared TIMMI camera by Lagadec et al. (2005), revealing a hot spot offset from the star, 0.9″ in the north-east direction. Additionally, interferometric observations with higher angular resolution in the same infrared band were also performed. Townes et al. (2011), using short-baseline (4 m to 35 m) configurations, detected a central source dominated by an extended environment with a radius of about 280 mas. Zhao-Geisler et al. 2012, using baselines ranging up to 70 m, confirmed the extended background and reported the complexity of the data at larger baselines.

In this paper, we report the first polychromatic images of the star V Hya and its close environment (between 1 and 10 stellar radii) obtained from interferometric observations in the L and N bands. The paper is structured as follows: in Sect. 2, we summarize the observational setup and the data-reduction procedure. In Sects. 3 and 4, we describe the visibility fitting and the image reconstruction strategy, respectively. In Sect. 5, we fit the spectral energy distribution of V Hya to derive the dust properties of the circumstellar environment. In Sect. 6, we present our main results, including the images of V Hya and its complex circumstellar environment. In Sect. 7, we discuss the origin of the geometry of the circumstellar environment and the asymmetric structures within it. In Sect. 8, we provide concluding remarks.

2. Observations and data reduction

2.1. MATISSE data

The main dataset presented in this paper was obtained using the Multi Aperture Mid-Infrared SpectroScopic Experiment (MATISSE) instrument (Lopez et al. 2022). MATISSE works simultaneously in three infrared bands: L (3.0 to 4.0 μm), M (4.5 to 5.0 μm), and N (8 to 13 μm). It combines the beams of four telescopes of the Very Large Telescope (VLT; at Cerro Paranal, Chile). These telescopes are either Unit Telescopes (UT; 8 m aperture) or the Auxiliary Telescopes (AT; 1.8 m aperture). The AT telescopes can be moved on the VLT platform. They span baselines from about 12 up to 140 m[2]. These configurations allow us to cover different regions in the (u, v)-plane, reaching an unprecedented angular resolution in the L ($\lambda/2B_{\max}$ = 2.2 mas, at λ = 3 μm and $B_{\max}$ = 140 m), and in the N band (up to 7 mas at λ = 10 μm).

The target V Hya was observed during the first semester of 2022 as part of the Large Program 108.22E9. The complete journal of observations can be found in Table A.1. The goal of the program is to image the overall geometry of the various targets, hence the L- and N-band low spectral resolution (R = 30) setup was chosen. The L-band data of V Hya were obtained using the slow-detector reading speed and a detector-integration time (DIT) of 0.075 s with central wavelength 3.5 μm. At the time of the observations, this detector setup was the only one optimised to cover entirely the C_2H_2+HCN absorption features in the spectrum of C-rich AGB stars (Jørgensen et al. 2000). However, it was limited to the wavelength range 2.85–4.20 μm and did not allow us to observe at the M band. The data analysis presented here starts at 3 μm because data at shorter wavelengths are too noisy. The N band data were taken with the only detector mode available for the low spectral resolution setup (high gain and DIT= 0.020 s), allowing us to cover the full N-band wavelength range.

The time interval between the first and last observation night was 93 days, corresponding to a phase span of 0.17 (over the 530-day pulsation period; Knapp et al. 1999). As we demonstrate below, based on the integration of the radial velocity curve to derive diameter variations, this variation remains below the resolution of MATISSE as long as the time span does not exceed one-fifth of the period. As a consequence, the effect of the pulsation is ignored in the data analysis, and all the data are merged together. The peak-to-peak radial velocity amplitude measured in the optical is about 10.7 km s^{-1} over the pulsation cycle (Barnbaum et al. 1995). Assuming the radial pulsation

[1] Andriantsaralaza et al. (2022) reported that the uncertainties on *Gaia* distances for red stars are underestimated by up to a factor of 5. Hence, caution should be exercised when converting parallaxes into distances by a simple inversion because the parallax resulting from this inversion becomes largely biased when the parallax fractional error is larger than 0.2 (Bailer-Jones 2015).

[2] Since 2023, the 200 m baseline configuration is offered to the community.

follows a sinusoidal evolution, this velocity amplitude would correspond to a variation in stellar radius of about 0.5 au over the entire cycle (Planquart et al. 2024). The radius evolution during the MATISSE observing span would correspond to ±0.3 mas (taking a distance of 340 pc as a lower boundary), which is well below the angular resolution of the MATISSE observations. Additionally, estimates of the radius variation for AGB stars in the thermal infrared through interferometric measurements were performed by Zhao-Geisler et al. (2011) for the SRa/Mira star W Hya. Zhao-Geisler et al. (2011) concluded that the diameter variation (5.4±1.8 mas) between visual minimum and maximum depends weakly on pulsation. Translating this into the distance of V Hya (the distance of W Hya is estimated to be about 98^{+30}_{-18} pc; Vlemmings et al. 2003), an overall diameter variation of 1.8±0.6 mas would be expected, in accordance with the estimates obtained from the variation in the radial velocity observations.

Each observing block of the science target was preceded and/or followed by the observation of a calibrator star. Table A.2 lists the calibrators, the spectral type, their *L*- and *N*-band diameters, and their corresponding fluxes. The raw data were processed using the Python tools mat_tools[3] provided by the MATISSE consortium. The Python interface encompasses the standard ESOREX (version 3.13.5) data-reduction tool for ESO/MATISSE. The data reduction was performed following the standard steps described in Drevon et al. (2022a). Due to the different geometrical setups for the *N*- and *L*-band detectors, the phase convention of the *N* band was flipped with respect to that of the *L* band. As of version 1.5.2 of the DRS, this results in a sign inversion for the *N*-band closure phase, and hence, in a 180° rotation in the final reconstructed images (see Sect. 4.8 in Gámez Rosas et al. 2022). The images presented in this paper have been rotated accordingly to project them correctly onto the sky plane.

Figure B.1 shows the squared visibilities and closure phases as a function of the spatial frequencies. The plot of the squared visibility shows a lack of data points above the 0.3 level in both bands, which is due to the presence of an extended thermal emission background that is over-resolved by the instrument. The closure phase plot exhibits a non-zero signal, revealing that the source is not centro-symmetric.

2.2. VISIR data

For a complementary view of V Hya in the *N* band, we also used archival data from the VLT mid-infrared spectro-imager VISIR (Lagage et al. 2004). V Hya and the point spread function calibrator (hereafter PSF) HD 93813 were observed on 30 January 2016 (Program: 096.D-0568) in coronographic imaging mode (λ_0 = 11.3 µm, $\Delta\lambda$= 0.5 µm, filter name = 11_3_4QP).

The annular groove phase mask coronagraph optimized for working in the *N* band was used (Delacroix et al. 2012). The total point source rejection of this type of vortex coronagraph is typically about 50. The observational procedure was identical to standard imaging, that is, chopping and nodding in parallel mode to suppress the large thermal background. After the chopping/nodding correction, the resulting images were background-noise limited. A total integration time of 600 s was dedicated to V Hya, half of which was spent with the object under the coronagraph (the rest of the time, the object was out of the coronagraph center due to the chopping/nodding sequence). After a standard data reduction using a custom-made pipeline (Pantin 2010), the high-level datacubes were analysed and sorted out. The worst frames (based on centring under the coronagraph and point source leaks) were rejected using an automatic selection algorithm. Several levels of rejection yield (30%, 60%, and 90%) were tested, and the resulting images can be found in Appendix F. A visual inspection of the results after frame selection showed very similar structures, and the rejection yield with the best signal-to-noise ratio (90%) was retained so that the final image was obtained by disregarding the 10% worst frames of the datacube. This image was then corrected for PSF residuals using observations of the standard star HD93813, which is assumed to be a point source. The final data were then flux calibrated using the standard star (from the infrared calibrators list of Cohen et al. 2003), where HD 93813 was assumed to have a flux density of 27.83 Jy in the filter used.

[3] Freely available at https://gitlab.oca.eu/MATISSE/tools

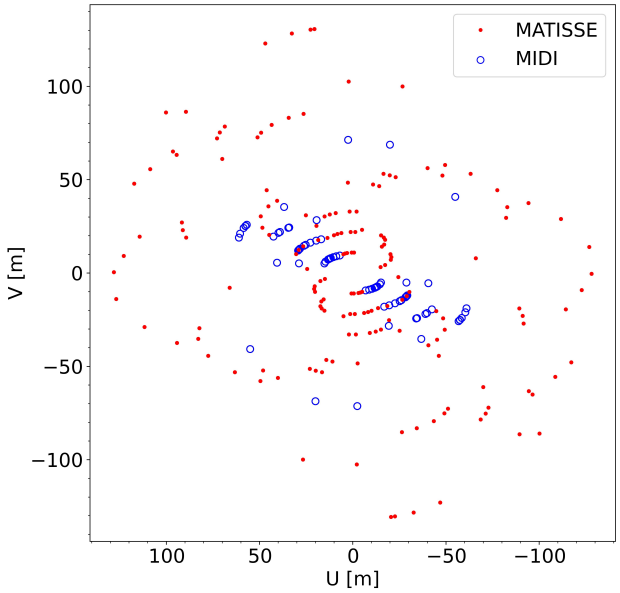

Fig. 1. (u, v)-plane coverage of MATISSE (red dots) and MIDI observation (open blue circles). U and V represent the coordinates of the sky-projected baseline vectors (expressed in meters).

2.3. MIDI data

V Hya has been observed over the years by various instruments. Zhao-Geisler et al. (2012) presented VLTI/MIDI (Leinert et al. 2003) data that are quite relevant for the current study. MIDI, the predecessor of MATISSE, was a two-telescope beam combiner observing in the *N* band with similar spectral setups as MATISSE. The MIDI data from Zhao-Geisler et al. (2012) are in low spectral resolution (R = 30), and they were taken with various baselines and orientations as shown in Fig. 1. The observations were carried out between the end of 2007 and 2009, about 13 yr before the MATISSE observations. In Fig. 2, the epochs of the observations are superimposed on the visual light curve of V Hya from the American Association of Variable Star Observers (AAVSO, Kloppenborg 2023). These data are used in the following sections to help in the scientific interpretation of the MATISSE data.

As shown in Fig. 2, the observations taken by the three instruments sample different epochs. The respective 530 days pulsation and 17 yr obscuration phases ($\varphi_{\rm puls}$, $\varphi_{\rm obs}$) are (0.00−0.57, 0.32−0.34) for MIDI, (0.91, 0.73) for VISIR, and

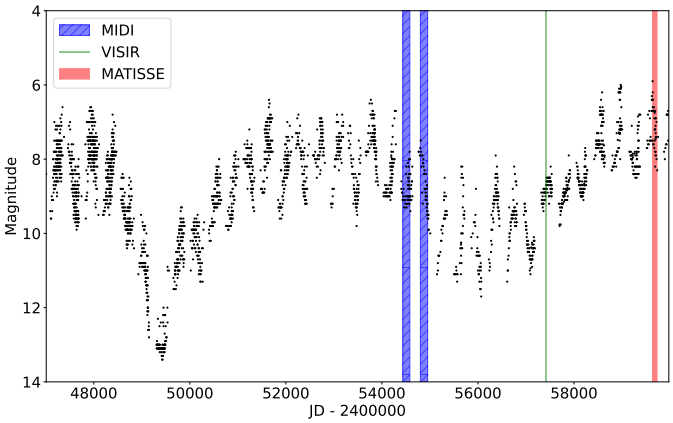

Fig. 2. AAVSO light curve of V Hya in the visual band (black points). The blue rectangle corresponds to the MIDI epoch of observation, the green line to the VISIR epoch, and the filled red rectangle to the MATISSE epoch.

Table 1. Dusty circumstellar envelope parameters for V Hya obtained with DUSTY.

Parameter	Value
Chemical composition	90 ± 5% AmC 10 ± 5% SiC
Grain distribution	$n(a) \propto a^{-3.5}$
Shell relative thickness, Y	10 000
Inner radius, $R_{\rm in}$ (au)	20 ± 2
Inner boundary temperature, $T_{\rm in}$ (K)	1050 ± 90

(0.10–0.27, 0.08–0.1) for MATISSE. The zero-phase of each cycle was taken as the closest light-maximum.

3. Parametric modelling of the visibility

As a first step, the interferometric data were interpreted using a parametric-model approach. As the visibility curve is complex, a simple geometrical model (i.e. Gaussian, uniform disc) cannot fit the data completely, but it provides a first characterisation of the general geometry of the object. The GEometrical Model Fitting for INterferometric Data (GEM-FIND; Klotz et al. 2012) software fits the visibility data with composite geometrical models using a Levenberg-Marquardt minimisation method (see Markwardt 2009). Five models with one or two components were tested in this work: (1) an elliptical Gaussian, (2) an elliptical uniform disc, (3) a detached shell model composed of a uniform disc and a ring, (4) a binary model composed of two uniform discs, and (5) a combination of an elliptical Gaussian and a uniform disc of a given radius. GEM-FIND is designed for N-band analysis and was applied to both MIDI and MATISSE data. This tool was preferred over other available geometric-model tools because it was specifically designed to read text files such as the old MIDI pipeline output[4]. The results, summarised in Table 2, are discussed in Sect. 6.1.

The second tool we used for the parametric interpretation is called Reconstructing Hankel rAdial Profiles in centro-Symmetric Objects with Discrete rings for astrophYsics (RHAPSODY; Drevon et al. 2022b). It reconstructs the visibility with a set of concentric discrete uniform rings using a reduced chi-squared and Bayesian minimisation method. The relative weight of the constraints from the measurements and those set by the prior is controlled by the so-called hyperparameter.Additionally, the method uses two angles of rotation (inclination and position angle) to add an angular dependence to the visibility profile, transforming the circular rings into elliptical ones.

The MATISSE closure phase is non-zero and non-π, implying strong asymmetries in the brightness distribution that cannot be modelled by fitting the visibility curve alone. The non-centrosymmetric signature can be retrieved with image-reconstruction methods that are able to simultaneously fit the visibility and the closure phase signal.

[4] The MIDI pipeline also delivered a first version of OIFITS, but they are not available for the V Hya data.

Table 2. Results of the visibility fitting for the best GEM-FIND model and RHAPSODY-reconstructed intensity profile.

GEM-FIND	MIDI	MATISSE
λ (µm)	11.35	11.35
PA (°)	160 ± 10	71 ± 20
Axis ratio	0.7 ± 0.1	0.8± 0.2
Brightness ratio	4.9 ± 0.1	5.5 ± 0.3
FWHM (mas)	21.3± 0.2	16.4 ± 0.5
χ^2	29	3.68
RHAPSODY	**MATISSE**	**MATISSE**
λ (µm)	3.66	11.35
PA (°)	150	65
Axis ratio	0.5	0.7
Hyperparameter	10^4	5×10^4
χ^2	2.18	2.74

Notes. PA is the position angle, counted from North to East. The brightness ratio is between the uniform disc and the Gaussian.

4. Image-reconstruction procedure

The (u, v)-plane coverage obtained from our observations (see Fig. 1) is dense and spatially well distributed, making the MATISSE interferometric observables suitable for the use of image-reconstruction techniques. The images were reconstructed using SQUEEZE (Baron et al. 2010), based on simulated annealing as minimisation engine. The images were obtained by the following procedure: 50 chains were initialised on a different random image and were run for 6000 iterations, using the transpectral regularizer. The final image was the mean image over the 50 chains. Images at one standard deviation from the mean display the same overall features (see Fig. C.1). The image size was set to 128 × 128 pixels, and the resolution was set to 1 mas for the L-band and 2 mas for the N-band. Four wavelength intervals, probing different molecular- and/or dust-forming regions have been selected to produce images (see Fig. 3): 3.15−3.20 µm (in C_2H_2+ HCN absorption band), 3.60–3.65 µm (in the L-band pseudo-continuum), 10.50–10.55 µm (in the N−band pseudo-continuum), and 11.45–11.50 µm (near the SiC emission peak). Images reconstructed in a narrow wavelength range ($\Delta\lambda$ = 0.05 µm) are needed to detect a wavelength-dependent structural change in the source morphology. On the other hand, images reconstructed in a larger spectral band (here $\Delta\lambda$ = 1 µm) allow us to constrain with an increased precision geometrical features as more interferometric observables are fitted simultaneously. For the N band, we also reconstructed

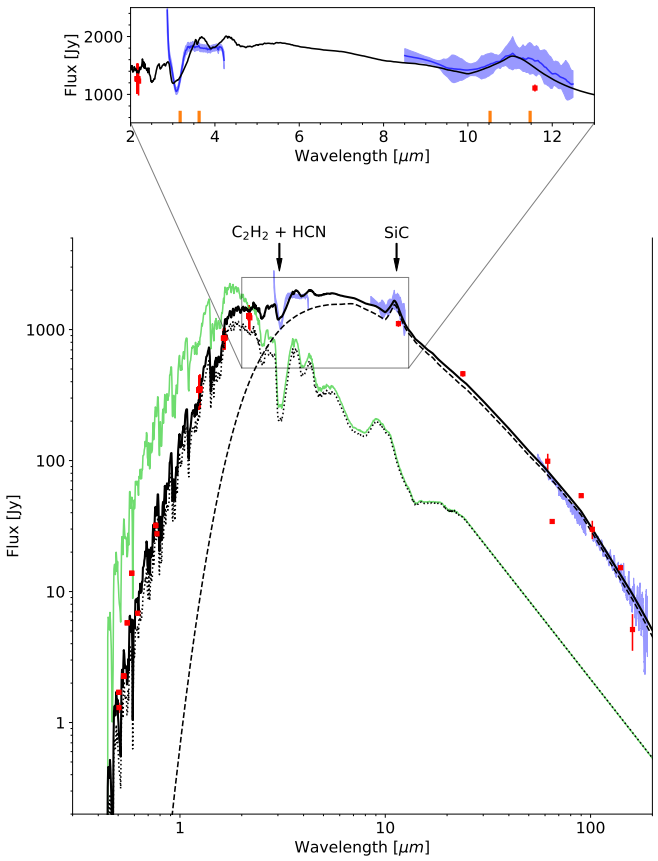

Fig. 3. Spectral energy distribution of V Hya. The red dots represent the photometric data from Table E.1. The blue shades from left to right are, the MATISSE (L and N bands) and the HERSCHEL-PACS spectrum. The green line is the (unreddened) COMARCS stellar spectrum. The dotted line represents the reddened spectrum. The dashed line is the contribution of the dust emission and the thick black line represents the resulting DUSTY model. The inset zooms onto the MATISSE spectra. The vertical orange bars mark the wavelength region selected for image reconstruction.

images for the interval 10.50−11.50 μm, by simultaneously fitting 2016 square-visibility points and 1343 closure phase points, for a final χ^2_r of 1.86.

To assess the reliability of the images obtained with SQUEEZE, two additional reconstruction packages were used: MIRA by Thiébaut (2008) and IRBis by Hofmann et al. (2014). The detailed procedure is described in Appendix C. The final images obtained with the three methods are displayed in Fig. C.3, where they are convolved with a theoretical point spread function using a Gaussian with a full width at half maximum (FWHM) equal to the interferometer resolution $\lambda/2B_{\max}$. The images are found to be similar, revealing the convergence of the reconstruction process. As a last validation step, we performed a reconstruction with SQUEEZE on a simulated dataset to quantify the impact of the limited (u, v)-coverage on the image quality. The simulation step allowed us to obtain an estimate of the feature arising from reconstruction artefacts. The results of the simulations are detailed in Appendix D.

5. Modelling the spectral energy distribution

In this section we perform a qualitative study of the spectral energy distribution (SED) of V Hya using a composite model, following the approach of Sacuto et al. (2011).

This analysis was performed in the first place to later interpret the MATISSE photometric and interferometric data and compare the model prediction with the infrared images. As the star undergoes a photometric variability (see Sect. 1), deriving precise stellar parameters from the fitting process of the optical region is not possible with the available photometry. We therefore first selected a carbon star hydrostatic model compatible with the properties of V Hya from literature. This synthetic spectrum was used as input radiation in the 1D radiative-transfer DUSTY code to model the effect of a dusty environment on the spectral energy distribution (Ivezic & Elitzur 1997).

5.1. Photometric data

The calibrated MATISSE spectra are shown in the spectral energy distribution (Fig. 3) together with the HERSCHEL-PACS[5] spectrum and photometric data (listed in Table E.1) To correct the photometric data for the interstellar reddening, the visual extinction equation is estimated using the tri-dimensional maps of the interstellar matter (Lallement et al. 2019) and the extinction curves of Gordon et al. (2009) were adopted. The extinction value in the visual is 0.09, and the impact of the interstellar extinction is negligible in the infrared.

5.2. Hydrostatic model

To reproduce the stellar contribution to the total flux, we used the synthetic COMARCS[6] spectra (Aringer et al. 2009). The COMARCS spectra are computed from 1D hydrostatic models and take the absorption by atomic and molecular species from the Copenhagen Opacities for Model Atmospheres (COMA) opacity tables into account. Further information about the COMA code and COMARCS spectra can be found in Aringer et al. (2009) and Lederer & Aringer (2009). From the available COMARCS spectra, we selected an input spectrum compatible with the V Hya inferred properties: temperature of 2700 K (Knapp et al. 1997), a C/O ratio of 1.05 (Lambert et al. 1986) and a mass of 1 $M_\odot$ (Kahane et al. 1996). The other fixed parameters of the COMARCS model were a surface gravity $\log g$ of –0.4 and solar metallicity. The final C/O ratio is 1.4 (see Sect. 5.3), which is well above the value 1.05 obtained by Lambert et al. (1986).

5.3. Dust contribution

To account for the dust contribution of the circumstellar environment, the 1D radiative transfer code DUSTY[7] (Ivezic & Elitzur 1997) was used. This 1D approach constitutes a simplistic approximation, but is justified by the fact that the MATISSE and VISIR images we present (see Fig. 7 in Sect. 6.4) show no strong asymmetric signatures, which are instead observed at different wavelengths (see Sect. 1). The main purpose of the DUSTY modelling was to provide a first approximation of the dust parameters and composition and to calibrate the flux of the images. A multi-dimensional modelling of the system is beyond the scope of this paper.

DUSTY solves the radiative transfer problem in a circumstellar environment assuming spherical symmetry. For AGB stars, the density distribution is assumed to be driven by the pressure on dust grains, which produces winds, known as radiatively-driven winds (Höfner & Olofsson 2018). The dust grain-size

[5] http://archives.esac.esa.int/hsa/whsa/
[6] http://stev.oapd.inaf.it/synphot/Cstars/
[7] http://faculty.washington.edu/ivezic/dusty_web/

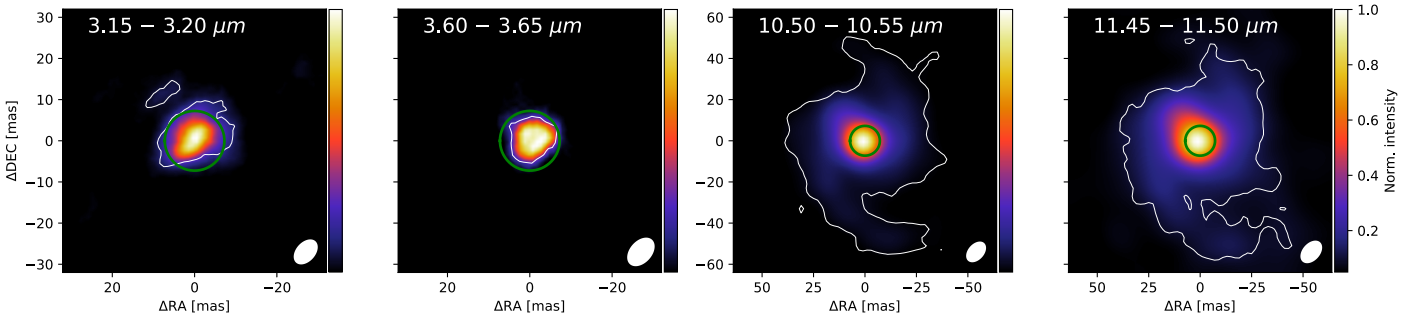

Fig. 4. MATISSE images of V Hya reconstructed with SQUEEZE at four different spectral ranges across the *L* and *N* bands. The green circle represents the expected star diameter of 14.5 mas as measured in the *K* band (Millan-Gabet et al. 2003). The white contour is drawn at 3σ (as described in Appendix C). The white ellipse in the bottom right corner represents the mean synthesised primary beam.

distribution was assumed to follow the standard MRN power law (Mathis et al. 1977) for the grain radius, a, ranging from 0.005 μm to 0.25 μm. The dust shell density is assumed to vary as $\rho(r) \propto r^{-2}$. For carbon stars, the grain mixture is expected to be mainly composed of amorphous carbon, AmC (Rouleau & Martin 1991), with a small contribution of silicon carbide, SiC (Pegourie 1988).

To derive the uncertainty of the input parameters AmC/SiC ratio, inner radius, and shell thickness, we assessed their impact on the SED. The adopted AmC/SiC ratio is 90/10, and a variation by ±5% of the SiC fraction does not allow us to reproduce the shape of the 11.3 μm SiC feature. The inner radius of the circumstellar envelope (CSE) is upper bounded by the location of the dust grain temperature of T = 1300 K, as found for IRC +10216 (Danchi et al. 1994). To correctly fit the *L*- and *N*-band fluxes simultaneously, an inner boundary located at 20 au is required, corresponding to an inner boundary temperature of 1050 K. Temperatures above 1200 K would lead to a lack of flux in the MATISSE bands, while temperatures below 950 K imply a flux excess in the *N*-band compared to the *L*-band. The value adopted for the temperature at the inner CSE boundary (thus fixing correspondingly the value of the inner radius) was taken in between the two threshold values mentioned above.

The geometrical thickness of the CSE was arbitrarily set to 10 000 inner radii of the dust shell. Values ranging from 100 to 10^5 have no significant impact on the SED for wavelengths below 100 μm (Sargent et al. 2010). Finally, the C/O ratio of the COMARCS model was fine-tuned to reproduce the absorption feature around 3.15 μm. The values are summarized in Table 1.

The composite COMARCS+DUSTY model is displayed in Fig. 3, together with the photometric data. The bolometric flux obtained is 3×10^{-9} W m^{-2}, corresponding to a stellar luminosity of L = 18 000 $L_\odot$ for the adopted distance of 434 pc.

Longward of 1.7 μm, the dust emission becomes the main contributor to the overall flux and dominates in the thermal infrared range (*L* and *N* bands).

6. Mid-infrared results

In this section, we first present the results of the parametric modelling of the visibility curves for the MATISSE and the MIDI data. Then we present the reconstructed images obtained for the MATISSE data. The latter are then used to assess the temporal variability in the visibility data between the two epochs. Finally, the MATISSE *N*-band image is flux calibrated and compared with the VISIR coronagraphic image to obtain the large-scale information of the CSE.

6.1. Visibility fitting

The results of the parametric modelling for MATISSE and MIDI are summarised in Table 2.

The best GEM-FIND model for both MATISSE and MIDI is composed of an over-resolved uniform disc (with a diameter fixed to 500 mas to mimic a background component) and an elliptical Gaussian. The extended uniform disc contributes 80% of the total flux. These values are consistent with the low visibility observed at small baselines (Fig. B.1), revealing an extended object that is fully resolved by the instrument. This ratio is similar to that previously found by Zhao-Geisler et al. (2012) using circular models (a uniform disc and a Gaussian) to fit the MIDI data: a central source of radius 19.3 ±3.5 mas that contributes 23% of the total flux. The FWHM of the central elliptical Gaussian, its brightness ratio, and its axis ratio, listed in Table 2, reveal similar values for the MIDI and MATISSE data. The elongation is well pronounced, resulting from the dependence on position-angle of the visibility. Remarkably, the position angle (PA, counted from north to east) of the major axis we obtained is shifted by about 90° between the two datasets. This change in the ellipse orientation between the two epochs is discussed in Sect. 7. The reconstructed intensity profile obtained with RHAPSODY at 11.35 μm and the model obtained with GEM-FIND for the same wavelength exhibit the same geometry: an elongated structure in the north–east direction with an axis ratio of 0.7 (Table 2). In the *L* band at 3.66 μm, the elongation is perpendicular to the one obtained in the *N* band.

In summary, the geometry of the central source depends on the position angle, but the two infrared bands do not share the same PA for their elongation axis. For the *N* band, the PA is not stationary on a 13-yr timescale. The temporal evolution of the *N*-band observables is further discussed in Sects. 6.3 and 7.2.

6.2. MATISSE images

The images obtained with SQUEEZE at four selected wavelength ranges are shown in Fig. 4. Their corresponding visibility and closure phase fits are displayed in Fig. B.1.

6.2.1. *L* Band

The image at 3.15–3.20 μm (leftmost panel of Fig. 4) probes the C_2H_2 and HCN absorption features. At these wavelengths, the image we obtained shows an elongated central source with an extension visible in the north-east quadrant. At 3.60−3.65 μm (second leftmost panel of Fig. 4), falling within the pseudo-continuum (see the inset in Fig. 3), the central source does not

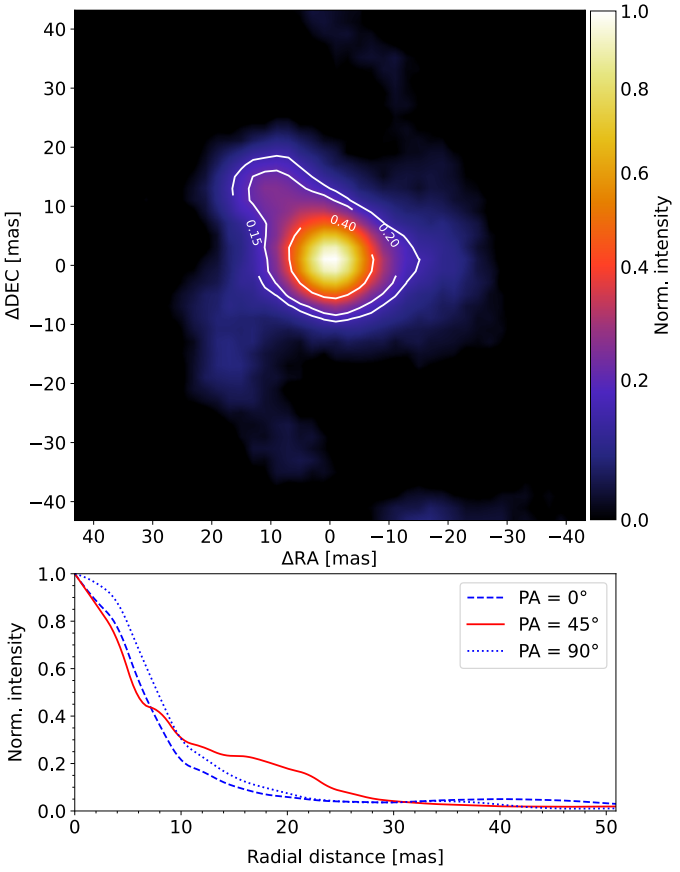

Fig. 5. MATISSE image of V Hya for the spectral interval 10.50–11.50 µm. Top: Image reconstructed with SQUEEZE. The white contour levels, labelled with the fraction of the peak intensity, highlight the elongation towards the upper left corner. In the text, this feature is referred to as the "20 mas extension". *Bottom*: radial cuts (starting from the central brightest pixel) in the image for different PAs, as indicated.

exhibit a circular shape either: an hook-like extension is directed toward the north-east quadrant and the central source diameter is smaller than the estimate from the *K*-band Millan-Gabet et al. (2003). The interpretation of these features is presented in Sect. 7.

6.2.2. *N* band

The *N* band images at 10.50−10.55 µm and 11.45–11.50 µm (Fig. 4, right panels) are displayed with a field of view twice larger to fully characterise the circumstellar environment. Both images exhibit a similar geometry: A central source with a diameter of about 14 mas (enclosed in the green circle, and corresponding to a fractional intensity of 0.7) and an extended emission in the north-east quadrant, hereafter referred as the "20 mas extension", whose PA is consistent with the elongation axis found from our preliminary model fitting (see Table 2). Comparison of the angular extension of the circumstellar dust in the two rightmost panels of Fig. 4 reveals that the source appears to be more compact at 10.50 µm than at 11.45 µm.

The image in the 10.50–11.50 µm band displayed in Fig. 5, together with the contour levels and the radial cuts at PAs of 0°, 45°, and 90°, illustrate the strong angular asymmetries (Fig. 9, discussed in Sect. 7.2 below, presents the same data, but in the form of a *L*- and *N*-band colour-composite image).

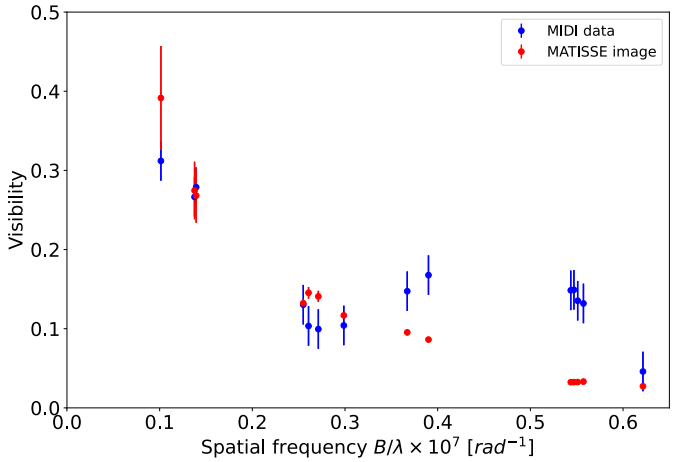

Fig. 6. Visibility measurements at 11.45 µm at phase ϕ_{puls} = 0.18±0.08. The blue points are the MIDI measurements from Zhao-Geisler et al. (2012). The red points are extracted from the MATISSE-reconstructed image at the (u, v)-coordinates of MIDI (see Fig. 1).

Given the simulations described in Appendix D, we may state that the spiral-like structure appearing in the *N*-band (best visible in the rightmost panel of Fig. 4 and to a lesser extent in Fig. 5) is likely an artefact of the image-reconstruction process related to the specific (u, v)-plane coverage.

6.3. Multi-epoch analysis of the visibility curve

The MIDI and MATISSE observations probe the same wavelength band but are separated in time by about a decade (see Fig. 2). Their (u, v)-plane coverage being slightly different in terms of PA or baseline lengths (see Fig. 1), a direct comparison of the visibility measurements is not straightforward. In Sect. 6.1, we fitted the visibilities using simple geometrical models and showed that the best-fitting models are not oriented along the same direction at the two epochs. To ensure that this difference is not an artefact of the different (u, v)-coverages, we extracted from the MATISSE-reconstructed image the visibilities at the exact (u, v)-coordinates of the MIDI observations. To eliminate the effect of pulsation, only the MIDI observations matching the pulsation phase of MATISSE (ϕ_{puls} = 0.10–0.27) were selected. The extrapolated visibility curve obtained from the MATISSE *N*-band image and the MIDI data are displayed in Fig. 6. The uncertainties on the synthetic MATISSE visibilities were extracted from the MEAN±STD image displayed in Fig. C.1. The general shape of the visibility curve strongly differs between the two epochs and is unlikely to originate from the flux variation induced by the pulsation.

6.4. Multi-scale analysis of the CSE

VISIR and MATISSE probe similar wavelength ranges but at different spatial scales. Figure 7 displays the coronagraphic image obtained with VISIR, together with the MATISSE *N*-band image at 11.45−11.50 µm. The field of view of VISIR is about 10 times larger than that of MATISSE. The VISIR image displays a circular emission pattern. The overall integrated flux (without the coronagraph) is equal to 1756 Jy, consistent with the MATISSE photometry (see Fig. 3). In the following we describe the procedure applied to calibrate MATISSE images in flux, as well as the comparison of the radial profiles of the images obtained from the two instruments.

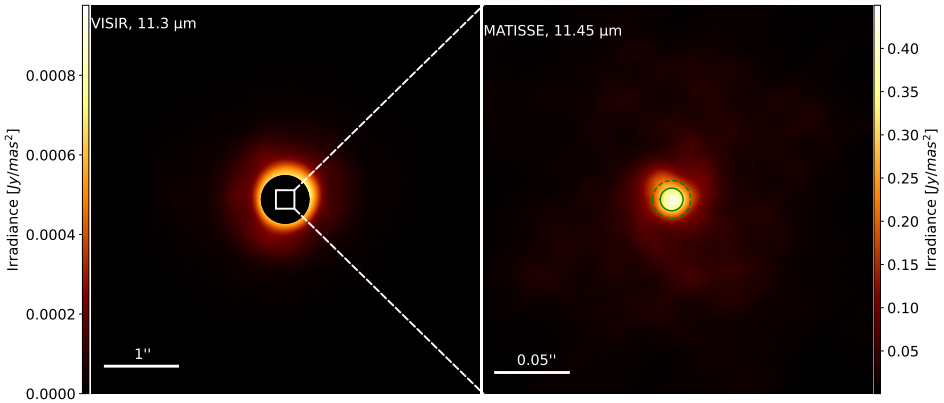

Fig. 7. VISIR-MATISSE comparison. *Left*: the VISIR coronagraphic images. *Right*: the corresponding MATISSE-reconstructed image. The scale of the MATISSE field of view is represented by a white rectangle at the centre of the VISIR image. The green continuous circle represents the size of the stellar disc as measured in the *K* band while the green dashed circle is its interpolated value in the *N* band (see text). North is up, and east is left.

As the MATISSE image is reconstructed from visibility and closure-phase measurements, each pixel value corresponds to its relative weight over the image and does not bear information about the absolute intensity of the source. To flux calibrate the image, we used as conversion factor the stellar flux from the SED computation (see Fig. 3, where the attenuated stellar radiation at 11.45 µm is 102 Jy). In the MATISSE image, only the pixels inside the photospheric radius contribute to the flux of the central component. The *N*-band uniform disc radius was derived by means of dynamic model predictions from the measured *K*-band value (7.25 mas from Millan-Gabet et al. 2003). A ratio of about 1.6 between the *K*- and *N*-band radii is expected for a carbon star with a stellar wind (Paladini et al. 2009), leading to an *N*-band radius of 12.3 mas. The *K*- and *N*-band radii are represented by the continuous and dashed green circles in Fig. 7.

The relative flux contribution of a central disc of 12.3 mas radius is 11% and corresponds to the stellar contribution plus an additional contribution from the dust emission located in the line of sight. The dust contribution was corrected for by removing the contribution of an annulus of half[8] the stellar area located just around the stellar radius. After implementing this correction, the stellar contribution drops to about 8% of the image flux density.

The radial intensity profile (averaged over the azimuthal angle) for the MATISSE *N*-band and VISIR images is displayed in Fig. 8. The two profiles are shown together with the radial profile from the DUSTY modelling (see the description in Sect. 5.3) for the same wavelength range. The good agreement between the model and the composite VISIR-MATISSE radial profile implies that the dust density profile roughly follows the r^{-2} trend adopted in the DUSTY model computation.

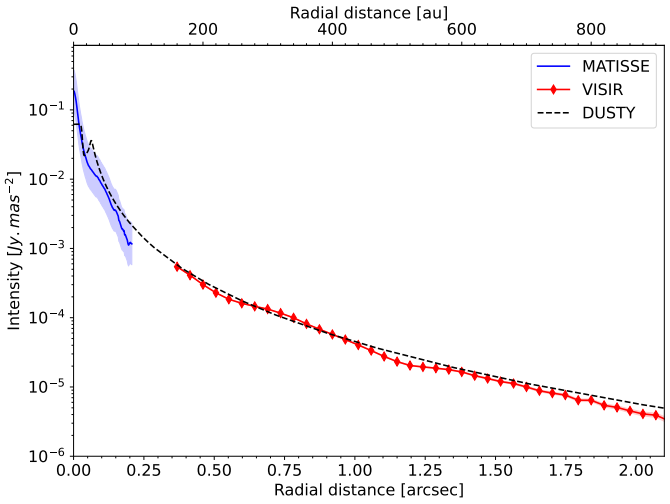

Fig. 8. Radial intensity cut of the 11.4 µm emission around V Hya, averaged over azimuthal angle. The MATISSE radial profiles (blue line, and its relative error represented by the shaded light blue area) are calibrated taking a photospheric radius of 12.3±5.0 mas. The VISIR radial profiles are displayed with square red symbols. The DUSTY model profile, downgraded to the MATISSE resolution, is displayed by the dashed black line.

7. Discussion

In this section, we interpret the features found in the MATISSE images, and discuss their properties and possible origin. We compare our interpretation with the signature predicted for a close-by companion, and finally, we discuss the overall shape of the dusty environment including the larger-scale image obtained from VISIR (see Fig. 7) and observations previously reported in the literature.

7.1. Morphology

7.1.1. Asymmetric stellar photosphere

As mentioned in Sect. 6.2.1, the images in the *L* band (Fig. 4) display an elongated structure (with a major axis oriented at about 150°, counted from north to east). Given the spatial scales of the asymmetries, they are likely to originate from the processes in the photosphere: The asymmetries are found within the expected angular radius of 7.25 mas (see Fig. 4). It is known from modelling that the dynamic process of pulsation and convection taking place in AGB stars can lead to surface-brightness asymmetries due to the presence of hot and cool convective cells on the photosphere (Chiavassa et al. 2011; Paladini et al. 2018). Previous near-infrared interferometric observations of the carbon-rich star R Scl show that the dimension of these cells can be up to one-third of the scale of the stellar photosphere with a brightness ratio of 1:2.5 (Wittkowski et al. 2017).

The shape of the stellar image in the *L* band also displays an extension in the north-east direction (see Fig. 4). This structure might also be related to the underlying convective atmosphere, like the structure observed in R Scl (Drevon et al. 2022a), but

[8] This factor 1/2 comes from the fact that we need to subtract the contribution of the dust located in front of the stellar disc using an annulus around the stellar disc that includes dust located both in front of and behind the star along these grazing lines of sight. When we assumed that the dust distribution is symmetric in front of and behind the factor 1/2 is justified, along with the fact that the dust is optically thin at the considered wavelengths (see Sect. 5.3).

in Sect. 7.2, we speculate that it might be linked to the binary companion.

7.1.2. North-east thermal emission

The images in the *N* band also display an elongation. However, in contrast to the *L* band, the major axis is oriented along the direction corresponding to the position angle of 45°, and is therefore perpendicular to the *L*-band major axis. As described in Sect. 6.4, the central emission is composed of a circular disc with a radius of ∼12 mas and a 20 mas extension in the north-east direction. The extension is more prominent at longer wavelengths. The SED modelling (see Sect. 5) shows that the *N*-band range is dominated by the dust emission. The dusty envelope is mainly composed of amorphous carbon, and silicon carbide causes the emission feature seen around 11.4 µm. As a consequence, the extension seen is likely to be related to the dust-forming region.

Two scenarios can be proposed to explain the origin of a dust clump located around the AGB star. It either an asymmetric ejection of material during the pulsation that cools down when pushed away from the AGB star, creating dust emission away from the central body in a random direction, as modelled by Höfner & Freytag (2019) and Freytag & Höfner (2023). The other explanation which we tend to favour given the binary nature of the star (see Sect. 1), is a dust clump induced by the presence of the close companion. Mohamed & Podsiadlowski (2012) and Chen et al. (2020) (to cite just a few) modelled the outflows from detached Mira-type binaries as wind Roche-lobe overflow (WRLOF). The simulations led to the creation of complex and asymmetric structures shaped by the binary motion, with particle enhancement in the vicinity of the location of the companion . In the next section, we argue why the binary scenario is considered as more likely and compare the interferometric observables with the orbital model.

7.2. Impact of a companion

Planquart et al. (2024) proposed for V Hya an orbital solution with a period of 17.5 yr (compatible with the light-curve modulation), a low eccentricity, an inclination of about 40°, and a semi-major axis of about 11.2 ± 1.5 au (25.8 ± 3.5 mas at 434 pc), the companion is therefore expected to fall in the MATISSE field of view. More precisely, knowing that the orbital phase difference between the system superior conjunction (corresponding to the last dimming event) and the MATISSE observation is $\Delta\phi$ = 0.6, it is possible to estimate the position of the companion in 2022. The companion (V Hya B) is expected to be offset from the central source by about 20 mas with a position angle of 60° ± 20° or 120° ± 20°, depending on whether a clockwise or counter-clockwise motion around the AGB star is adopted (see Sect. 3.2 in Planquart et al. 2024). These two possible positions predicted for the companion at the epoch of the MATISSE observation and the corresponding orbital motion since the last superior conjunction are displayed in the colour-composite MATISSE image (Fig. 9). The north-east 20 mas extension, agrees with the prediction of the position of the companion for a clockwise orbital motion.

The clockwise orbital motion is also slightly preferred by the difference in the proper motions of V Hya between the latest two *Gaia* data releases (GDR2 and GDR3 at epochs 2015.5 and 2016.0, respectively). The proper motion curve in declination between the two epochs can be described by a linear trend with a negative slope (non-zero within a 75% confidence interval).

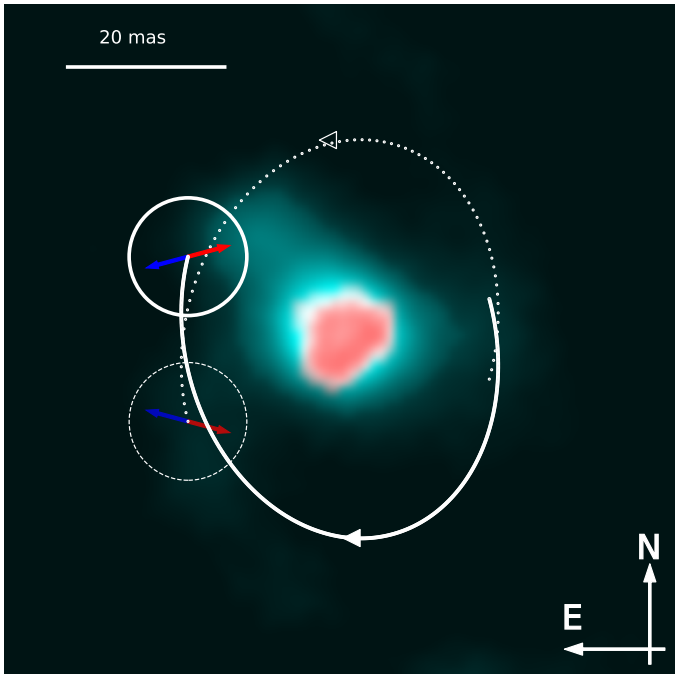

Fig. 9. Composite-colour image with the flux in *L* band (3.60 µm) displayed in red and flux in *N* band (10.50–11.50 µm) shown in blue. The solid white (dashed) circle represents the 3σ position prediction at MATISSE epoch for the clockwise (counter-clockwise) orbital motion. The white arcs show the path of the companion around the primary since the last superior conjunction, and the blue (red) arrow represents the sky-projected jet axis for the blueshifted (redshifted) direction.

This proper motion trend around the GDR2 and GDR3 epochs in turn corresponds to a declination sky-motion of V Hya following a downward-facing parabola, hence an opposite (upward-facing parabola) for the companion. This condition is met by the clockwise path in Fig. 9.

Additionally, the relation between the 20 mas extension and the companion orbital motion is supported by the PA of the elongation found in the earlier MIDI data. The MATISSE and MIDI datasets are separated by about 13 yr, and given the orbital period of 17.5 yr, this corresponds to a phase difference of 0.75. Considering that a full orbital revolution would induce a complete revolution of the 20 mas extension, the PA offset between the two epochs separated by 13 yr would be equal to 270°, in accordance with the PA values found by the model fitting (see Table 2).

The above arguments tend to favour the position prediction that matches the extension seen in the MATISSE *N*-band image. More precisely, since the companion is expected to be a main-sequence star, necessarily hotter than the AGB star (Sahai et al. 2008), it is supposed to be unresolved and not directly detectable in the infrared band (about a 1000 times fainter than the AGB star). The infrared emission observed close to the position of the companion would instead reveal particle (dust and molecules) enhancement. Chen et al. (2020) predict particle enhancement in the vicinity of the companion location, by up to three orders of magnitude above the ambient density.

The hook observed in V Hya *L*-band images (Fig. 4) points towards the unseen companion located north-east from V Hya (and 7 au farther away from the observer than the primary), suggesting a possible accreting flow, as imaged for Mira in the UV (Karovska et al. 2004). The north-east emission prominent in the *L*-band image taken in the C_2H_2 absorption feature (Fig. 4,

first panel) but not in the *L*-band image taken in the pseudo-continuum (Fig. 4, second panel) could correspond to a C_2H_2 enhancement close to the companion – C_2H_2 being a building block in the formation of amorphous carbon (Hanner 1988) and SiC (Pitman et al. 2008). It might also be an opacity effect that reduces the stellar contribution to the total flux in the molecular absorbing feature (see Fig. 5) and therefore increases the relative intensity of the clump.

The remaining open question concerns the structure (geometry and composition) of the clump and its possible connection with the periodic obscuration. The MATISSE *N*-band image confirms localised emission like this, but, as the image only gives us the sky-projected geometry of the emission region (seen as a 20 mas extension), no 3D geometry can be retrieved.

7.3. Link with the periodic obscuration

Constraints on the dust distribution in the system come from the light-curve shape and the system inclination: The dust clump should be opaque and extended along the jet axis to obscure the primary for about one-third of the orbital cycle and to cause obscuration up to $\Delta m = 3$ mag in the optical during the superior conjunction (see Fig. 2 and Planquart et al. 2024). The location of the obscuring cloud, above the orbital plane, cannot be easily explained by WLROF-type mass transfer, but it seems to require more sophisticated models involving jets, of the type encountered in pre-main sequence stars and post-AGB binaries (Ferreira et al. 2007; Verhamme et al. 2024).

The mass grain column density n required for the obscuration can be estimated through $\Delta m = 1.086\ n\ \kappa_{\rm ext}$, where $\kappa_{\rm ext}$ is the total extinction cross section per unit mass in the visible range. Assuming the Rayleigh regime, $\kappa^{\lambda}_{\rm ext}$ is given by $Q/a \times (3/4\rho)$ = $3{\times}10^4$ cm^2 g^{-1}, where ρ is the adopted mean grain density of 1.85 g cm^{-3} (Rouleau & Martin 1991), and Q/a (the extinction efficiency over the grain radius) is about 10^5 cm^{-1} at 0.55 µm (Andersen et al. 1999). Hence, a mass column density of about 10^{-4} g cm^{-2} would be required. This implies a total dust mass (contained in the absorbing cylinder located in the line of sight with an area subtended by V Hya photosphere with radius of 7.25 mas) of about $10^{-10}\ M_\odot$. During the dimming events, this amount of dust would alter the SED shape by inducing an additional absorbing source in the optical to near-infrared region.

The dust dynamics (dust cloud formed continuously or attached to the companion) cannot be retrieved with a single image of the dust-forming region. The only conclusion that can be drawn at this point is that a particle enhancement around the companion is present and that the obscuring dust clump should extend along the jet axis. Further observations in the infrared *N* band taken at a different orbital phase (e.g. during a dimming event) would constrain the geometrical structure of the 20-mas extension by probing the component positions from a different vantage point.

7.4. Large-scale morphology

The largest structure resolved by the MATISSE images is limited by the shortest baseline (∼15 m) of the interferometric measurements. As a consequence, any structure more extended than the largest recoverable scale ($\lambda/B_{\rm min}$ ∼ 165 mas at 12 µm) is not resolved. The low visibilities measured at the shortest baseline separation (see Fig. B.1) and the SED (Fig. 3) both confirm the extended dusty envelope. The large-scale geometry of the star has already been imaged in the thermal infrared with TIMMI in the *N* band (Lagadec et al. 2005) and with NACO in the *L* band (Lagadec et al. 2007). These observations, together with the VISIR coronagraphic image reveal an extended emission region (with a radius up to 2 arcsec). However, the limited angular resolution capabilities of the large-scale images do not allow the authors to resolve the innermost part of the structure. As a consequence, these observations only bring information on the extended structure and can be seen as fully complementary to the image provided by MATISSE.

One question that arises is the overall geometry of the CSE. If infrared observations favour an extended CSE (elliptical in the MATISSE field of view but nearly circular at larger scales), other observations at different wavelengths (e.g. Sahai et al. 2022) favour an overall geometry consisting of a combination of a bipolar high-velocity wind and an equatorial dense disc fed by a slow wind. This scenario is compatible with the different CO outflows found by Knapp et al. (1997) and with the high-velocity ejection (Sahai et al. 2016). More recently, the dense disc was revealed by asymmetric emission in near-infrared scattered light (Sahai et al. 2019). These two possible geometries (dense equatorial disc and/or high-velocity bipolar outflow) can neither be confirmed nor dismissed by the thermal infrared imaging (both MATISSE and previous observations).

The high-velocity gaseous bipolar outflow cannot be detected in the images because the low spectral resolution mode ($R = 30$) does not allow us to characterise the velocity structure of the emission, in contrast to what was done with Brackett lines in η Car where a spectral channel width of 20–40 km s^{-1} was achieved for Brγ in the *K* band and a width of 170 km s^{-1} for Brα in the *L* band (Weigelt et al. 2016, 2021, GRAVITY Collaboration 2018).

Regarding the presence of an equatorial density enhancement, given the low inclination of the system, such disc-like configuration emitting in the infrared would lead to a large emission region that is slightly elongated in a 2D image, making it indistinguishable from an elongated dusty CSE. If a disc causes for the extended emission instead of a CSE, it should be circumbinary. Discs like this are extensively found in post-AGB binaries (Kluska et al. 2022). As no signature of the disc is found in the MATISSE images, its inner radius should be located outside the field of view of the instrument.

8. Summary and conclusions

We presented the reconstructed images of V Hya in the thermal infrared obtained with the MATISSE instrument. We first modelled the spectral energy distribution using a composite model combining a hydrostatic COMARCS spectrum with DUSTY. It revealed that the star is surrounded by an extended dusty CSE, made of amorphous carbon and silicon carbide, which dominates the emission in the thermal infrared.

We performed a preliminary model-fitting of the visibility measurements. Then, we performed image reconstruction using the visibility and closure phase signals. The images of V Hya obtained from MATISSE interferometric measurements were processed using SQUEEZE, MIRA, and IRBis. In the *L* band, we presented the stellar photosphere in a molecular absorption band of C_2H_2-HCN and in the pseudo-continuum. We showed that both images display a non-spherically symmetric structure and explained it by photospheric material ejection. In the *N* band, we a north-east 20 mas extension to the stellar photosphere. We concluded that the extension arises from a dust enhancement whose position roughly matches the prediction for the position of the companion. We compared our MATISSE image with archive data from MIDI and observed changes in the interferometric data

between the two epochs, compatible with the orbital motion. Hence, the presence of a dusty clump around a companion is favoured compared to a blob ejected in a random direction by a single star. Finally, we compared the theoretical radial profile from the SED modelling with the observed composite radial profile constrained at the small scales by the MATISSE *N*-band image and at large scales by the images obtained with VISIR. We confirmed the extended dusty CSE around the central source. The high-velocity gaseous jet is not detected in the image, and a higher spectral resolution is required to resolve its origin and kinematic structure.

Future observations at different epochs would be of particular interest to retrieve temporal information about the dusty wind as a function of the orbital motion. This would provide strong constraints on the dust distribution around the binary components. Eventually, multi-dimensional radiative transfer reproducing the circumstellar and circumbinary environment of the V Hya system should be foreseen to connect the binary interaction to the large-scale morphology.

Acknowledgements. L.P. acknowledges an ESO studentship, and is FNRS research fellow. A.J. is supported by the *Fonds National de la Recherche Scientifique* (F.R.S.-FNRS) under PDR grant T.0115.23. S.H. acknowledges funding from the European Research Council (ERC) under the European Union's Horizon 2020 research and innovation programme (Grant agreement No. 883867, project EXWINGS) and the Swedish Research Council (Vetenskapsradet, grant number 2019-04059). F.L. received funding from the Hungarian NKFIH OTKA project no. K-132406. M.M. acknowledges funding from the Programme Paris Region fellowship supported by the Région Ile-de-France. This project has received funding from the European Union's Horizon 2020 research and innovation program under the Marie Skłodowska-Curie Grant agreement No. 945298. K.O. acknowledges the support of the Agencia Nacional de Investigación Científica y Desarrollo (ANID) through the FONDECYT Regular grants 1210652 and 1240301. This research has made use of the Jean-Marie Mariotti Center `Aspro` (`http://www.jmmc.fr/aspro`) and `OIFits Explorer` (`http://www.jmmc.fr/oifitsexplorer`) services. Use was made of the Simbad database, operated at the CDS, Strasbourg, France, and of NASA's Astrophysics Data System Bibliographic Services. This research made use of Numpy, Matplotlib, SciPy and Astropy, a community-developed core Python package for Astronomy (Astropy Collaboration 2018). We acknowledge with thanks the variable star observations from the AAVSO International Database contributed by observers worldwide and used in this research.

References

Andersen, A. C., Loidl, R., & Höfner, S. 1999, A&A, 349, 243
Andriantsaralaza, M., Ramstedt, S., Vlemmings, W. H. T., & De Beck, E. 2022, A&A, 667, A74
Aringer, B., Girardi, L., Nowotny, W., Marigo, P., & Lederer, M. T. 2009, A&A, 503, 913
Astropy Collaboration (Price-Whelan, A. M., et al.) 2018, AJ, 156, 123
Bailer-Jones, C. A. L. 2015, PASP, 127, 994
Barnbaum, C., Morris, M., & Kahane, C. 1995, ApJ, 450, 862
Baron, F., Monnier, J. D., & Kloppenborg, B. 2010, SPIE Conf. Ser., 7734, 77342I
Bergeat, J., Knapik, A., & Rutily, B. 1998, A&A, 332, L53
Bourges, L., Mella, G., Lafrasse, S., et al. 2017, JMMC Stellar Diameters Catalogue – JSDC. Version 2
Chen, Z., Ivanova, N., & Carroll-Nellenback, J. 2020, ApJ, 892, 110
Chiavassa, A., Pasquato, E., Jorissen, A., et al. 2011, A&A, 528, A120
Cohen, M., Megeath, S. T., Hammersley, P. L., Martín-Luis, F., & Stauffer, J. 2003, AJ, 125, 2645
Cruzalèbes, P., Petrov, R. G., Robbe-Dubois, S., et al. 2019, MNRAS, 490, 3158
Danchi, W. C., Bester, M., Degiacomi, C. G., Greenhill, L. J., & Townes, C. H. 1994, AJ, 107, 1469
Decin, L., Montargès, M., Richards, A. M. S., et al. 2020, Science, 369, 1497
Delacroix, C., Absil, O., Mawet, D., et al. 2012, in Ground-based and Airborne Instrumentation for Astronomy IV, Proceedings of the SPIE, Univ. de Liège (Belgium)
Doan, L., Ramstedt, S., Vlemmings, W. H. T., et al. 2020, A&A, 633, A13
Drevon, J., Millour, F., Cruzalèbes, P., et al. 2022a, A&A, 665, A32
Drevon, J., Millour, F., Cruzalèbes, P., Scicluna, P., & Paladini, C. 2022b, SPIE Conf. Ser., 12183, 121831O
Ferreira, J., Dougados, C., & Whelan, E. 2007, Jets from Young Stars I: Models and Constraints, 723
Freytag, B., & Höfner, S. 2023, A&A, 669, A155
Gaia Collaboration (Brown, A. G. A., et al.) 2021, A&A, 649, A1
Gámez Rosas, V., Isbell, J. W., Jaffe, W., et al. 2022, Nature, 602, 403
Gordon, K. D., Cartledge, S., & Clayton, G. C. 2009, ApJ, 705, 1320
GRAVITY Collaboration (Sanchez-Bermudez, J., et al.) 2018, A&A, 618, A125
Hanner, M. S. 1988, Infrared observations of comets Halley and Wilson and properties of the grains: summary of workshop sponsored by the National Aeronautics and Space Administration, Washington, D.C. and held at Cornell University, Ithaca, New York, August 10–12, 1987, NASA Conference Publication, ed. M. S. Hanner
Hirano, N., Shinnaga, H., Dinh-V-Trung, et al. 2004, ApJ, 616, L43
Hofmann, K. H., Weigelt, G., & Schertl, D. 2014, A&A, 565, A48
Höfner, S., & Olofsson, H. 2018, A&A Rev., 26, 1
Höfner, S., & Freytag, B. 2019, A&A, 623, A158
Ivezic, Z., & Elitzur, M. 1997, MNRAS, 287, 799
Jones, D., & Boffin, H. M. J. 2017, Nat. Astron., 1, 0117
Jørgensen, U. G., Hron, J., & Loidl, R. 2000, A&A, 356, 253
Kahane, C., Audinos, P., Barnbaum, C., & Morris, M. 1996, A&A, 314, 871
Karovska, M., Wood, B., Marengo, M., et al. 2004, Rev. Mex. Astron. Astrofis. Ser., eds. G. Tovmassian, E. Sion, et al., 20, 92
Kervella, P., Homan, W., Richards, A. M. S., et al. 2016, A&A, 596, A92
Kloppenborg, B. K. 2023, Observations from the AAVSO International Database, `https://www.aavso.org`
Klotz, D., Sacuto, S., Paladini, C., Hron, J., & Wachter, G. 2012, SPIE Conf. Ser., 8445, 84451A
Kluska, J., Van Winckel, H., Coppée, Q., et al. 2022, A&A, 658, A36
Knapp, G. R., Jorissen, A., & Young, K. 1997, A&A, 326, 318
Knapp, G. R., Dobrovolsky, S. I., Ivezić, Z., et al. 1999, A&A, 351, 97
Lagadec, E., Mékarnia, D., de Freitas Pacheco, J. A., & Dougados, C. 2005, A&A, 433, 553
Lagadec, E., Chesneau, O., Zijlstra, A. A., Matsuura, M., & Mékarnia, D. 2007, in Asymmetrical Planetary Nebulae IV, 16
Lagage, P. O., Pel, J. W., Authier, M., et al. 2004, The Messenger, 117, 12
Lallement, R., Babusiaux, C., Vergely, J. L., et al. 2019, A&A, 625, A135
Lambert, D. L., Gustafsson, B., Eriksson, K., & Hinkle, K. H. 1986, ApJS, 62, 373
Lederer, M. T., & Aringer, B. 2009, A&A, 494, 403
Leinert, C., Graser, U., Przygodda, F., et al. 2003, Ap&SS, 286, 73
Lloyd Evans, T. 1991, MNRAS, 248, 479
Lopez, B., Lagarde, S., Petrov, R. G., et al. 2022, A&A, 659, A192
Markwardt, C. B. 2009, Astronomical Data Analysis Software and Systems XVIII, eds. D. A. Bohlender, D. Durand, & P. Dowler, ASP Conf. Ser., 411, 251
Mathis, J. S., Rumpl, W., & Nordsieck, K. H. 1977, ApJ, 217, 425
Millan-Gabet, R., Pedretti, E., Monnier, J. D., et al. 2003, SPIE Conf. Ser., 4838, 202
Mohamed, S., & Podsiadlowski, P. 2012, Baltic Astron., 21, 88
Paladini, C., Aringer, B., Hron, J., et al. 2009, A&A, 501, 1073
Paladini, C., Baron, F., Jorissen, A., et al. 2018, Nature, 553, 310
Pantin, E. 2010, PhD thesis, CEA Saclay, Service d'Astrophysique
Pegourie, B. 1988, A&A, 194, 335
Pitman, K. M., Hofmeister, A. M., Corman, A. B., & Speck, A. K. 2008, A&A, 483, 661
Planquart, L., Jorissen, A., Escorza, A., Verhamme, O., & Van Winckel, H. 2024, A&A, 682, A143
Ramstedt, S., Mohamed, S., Vlemmings, W. H. T., et al. 2014, A&A, 570, L14
Rouleau, F., & Martin, P. G. 1991, ApJ, 377, 526
Sacuto, S., Aringer, B., Hron, J., et al. 2011, A&A, 525, A42
Sahai, R., & Wannier, P. G. 1988, A&A, 201, L9
Sahai, R., Findeisen, K., Gil de Paz, A., & Sánchez Contreras, C. 2008, ApJ, 689, 1274
Sahai, R., Sugerman, B. E. K., & Hinkle, K. 2009, ApJ, 699, 1015
Sahai, R., Scibelli, S., & Morris, M. R. 2016, ApJ, 827, 92
Sahai, R., Rajagopal, J., Hinkle, K., Joyce, R., & Morris, M. 2019, IAU Symp., 343, 495
Sahai, R., Huang, P. S., Scibelli, S., et al. 2022, ApJ, 929, 59
Sargent, B. A., Srinivasan, S., Meixner, M., et al. 2010, ApJ, 716, 878
Schlafly, E. F., Meisner, A. M., & Green, G. M. 2020, VizieR Online Data Catalog, II/363
Thiébaut, E. 2008, SPIE Conf. Ser., 7013, 70131I
Townes, C. H., Wishnow, E. H., & Ravi, V. 2011, PASP, 123, 1370
Tsuji, T., Unno, W., Kaifu, N., et al. 1988, ApJ, 327, L23
Verhamme, O., Kluska, J., Ferreira, J., et al. 2024, A&A, 684, A79
Vlemmings, W. H. T., van Langevelde, H. J., Diamond, P. J., Habing, H. J., & Schilizzi, R. T. 2003, A&A, 407, 213
Weigelt, G., Hofmann, K. H., Schertl, D., et al. 2016, A&A, 594, A106

Weigelt, G., Hofmann, K. H., Schertl, D., et al. 2021, A&A, 652, A140
Wittkowski, M., Hofmann, K. H., Höfner, S., et al. 2017, A&A, 601, A3
Zhao-Geisler, R., Quirrenbach, A., Köhler, R., Lopez, B., & Leinert, C. 2011, A&A, 530, A120
Zhao-Geisler, R., Quirrenbach, A., Köhler, R., & Lopez, B. 2012, A&A, 545, A56

[1] Institut d'Astronomie et d'Astrophysique, Université Libre de Bruxelles, CP 226, Boulevard du Triomphe, 1050 Brussels, Belgium
e-mail: lea.planquart@ulb.be
[2] European Southern Observatory, Alonso de Córdova, 3107 Vitacura, Santiago, Chile
[3] Instituto de Astrofísica de Canarias, C. Vía Láctea, 38205 La Laguna, Tenerife, Spain
[4] Universidad de La Laguna, Departamento de Astrofísica, Av. Astrofísico Francisco Sánchez, 38206 La Laguna, Tenerife, Spain
[5] Université Paris-Saclay, Université Paris Cité CEA, CNRS, AIM, 91191 Gif-sur-Yvette, France
[6] Université Côte d'Azur, Observatoire de la Côte d'Azur, CNRS, Laboratoire Lagrange, France
[7] Department of Astrophysics, University of Vienna, Türkenschanzstraße 17, 1180 Wien, Austria
[8] Center for High Angular Resolution Astronomy and Department of Physics and Astronomy, Georgia State University, PO Box 5060, Atlanta, GA 30302-5060, USA
[9] NASA Goddard Space Flight Center, USA
[10] Department of Space, Earth and Environment, Chalmers University of Technology, Onsala Space Observatory, 43992 Onsala, Sweden
[11] Royal Observatory of Belgium, Ringlaan 3, 1180 Brussels, Belgium
[12] Theoretical Astrophysics, Department of Physics and Astronomy, Uppsala University, Box 516, 751 20 Uppsala, Sweden
[13] Konkoly Observatory, Research Centre for Astronomy and Earth Sciences, Hungarian Research Network (HUN-REN), Konkoly Thege Miklós út 15–17., 1121 Budapest, Hungary
[14] LESIA, Observatoire de Paris, Université PSL, CNRS, Sorbonne Université, Université Paris Cité, 5 place Jules Janssen, 92195 Meudon, France
[15] Instituto de Astrofísica, Universidad Andrés Bello, Fernández Concha 700, Las Condes, Santiago, Chile
[16] Instituto de Astronomía, Universidad Nacional Autónoma de México, Apdo. Postal 70264, Ciudad de México 04510, Mexico
[17] Max Planck Institute for Radio Astronomy, Auf dem Hügel 69, 53121 Bonn, Germany
[18] European Southern Observatory (ESO), Karl-Schwarzschild-Str. 2, 85748 Garching bei München, Germany

Appendix A: Observation log

Table A.1 summarises the log of MATISSE observations for V Hya. Table A.2 lists the calibrators we used and their characteristics.

Table A.1: Observation log used for V Hya.

Date	Time [UT]	VLTI config.	Object	Seeing [″]	τ_0 [ms]	FT
2022-02-25	04:22:16	A0-G1-J2-K0	HD 98993	0.55	15.33	1
	04:44:46		V Hya	0.55	19.49	0.98
	04:58:09		α Hya	0.53	16.38	1
2022-02-27	06:43:12	A0-G1-J2-K0	HD 98993	0.41	11.98	1
	07:05:36		V Hya	0.35	12.10	0.99
	07:27:56		ϵ Crv	0.40	15.08	1
2022-02-28	05:21:38	A0-G1-J2-J3	HD 98993	0.55	8.02	1
	05:43:24		V Hya	0.67	5.41	1
	05:56:18		α Hya	0.61	6.45	1
2022-03-02	07:23:51	A0-G1-J2-J3	HD 98993	0.43	14.07	1
	07:48:21		V Hya	0.58	12.24	1
	08:02:42		ϵ Crv	0.54	13.09	1
2022-03-07	04:47:02	K0-G1-D0-J3	HD 98993	0.43	10.28	1
	05:06:53		V Hya	0.37	11.23	0.98
	05:23:09		α Hya	0.33	9.56	1
	05:45:10		HD 98993	0.28	10.63	1
	06:04:02		V Hya	0.31	8.60	1
	06:18:17		α Hya	0.30	13.54	1
2022-03-10	05:05:15	K0-G2-D0-J3	HD 98993	0.77	5.35	1
	05:16:55		V Hya	0.66	7.23	1
	05:45:46		ϵ Crv	0.45	12.58	1
2022-03-11	07:02:41	A0-B2-D0-J3	HD 98993	0.45	7.15	1
	07:22:25		V Hya	0.49	6.92	0.99
	07:46:13		ϵ Crv	0.38	7.93	1
2022-03-12	00:40:55	A0-B2-D0-C1	V Hya	1.26	3.00	1
	01:01:58		α Hya	1.25	2.32	1
	00:53:11		α Hya	1.26	2.08	1
	01:22:22		V Hya	1.11	2.47	1
	01:47:04		α Hya	1.05	3.18	1
	01:37:11		α Hya	1.02	3.23	1
	02:54:09		V Hya	0.85	3.32	1
	03:15:15		α Hya	0.82	4.41	1
	03:09:03		α Hya	0.83	3.32	1
	03:39:05		V Hya	0.84	5.47	1
	04:00:56		α Hya	0.83	5.62	1
	04:16:50		V Hya	0.93	4.44	1
	04:58:25		α Hya	0.92	4.47	1
2022-04-12	00:41:38	A0-G1-J2-K0	HD 98993	0.88	2.96	1
	01:01:04		V Hya	0.89	3.53	0.98
	01:23:31		ϵ Crv	0.63	4.30	1
2022-04-30	01:52:21	A0-B2-D0-C1	α Hya	1.32	4.55	1
	02:11:33		V Hya	0.91	8.83	1
2022-05-30	00:55:00	K0-G2-D0-J3	HD 98993	0.77	3.33	1
	01:16:24		V Hya	0.66	3.81	1
	01:36:40		ϵ Crv	0.79	3.28	1

Notes. The column labelled "VLTI config." refers to the AT stations, τ_0 is the coherence time in the visible and FT refers to the fringe tracking ratio, a FITS keyword providing the percentage of fringes tracked by the MATISSE master-band (L band in the specific case) during the observations. The latter is an indicator of the data quality.

Table A.2: List of the calibrator targets used.

Name	Spec. Typ.	θ_{UD} L [mas]	θ_{UD} N [mas]	F_L [Jy]	F_N [Jy]
HD 98993	K4	2.71 ± 0.33	2.73 ± 0.33	80 ± 2	12± 3
HD 81797 (α Hya)	K3	8.71 ± 0.63	8.79 ± 0.63	948 ± 48	70 ± 8
HD 105707 (ϵ Crv)	K2	5.25 ± 0.42	5.29 ± 0.42	283 ± 67	43± 12

Notes. The diameters of the calibrators are from the II/346 Vizier catalog (Bourges et al. 2017). Flux values from Cruzalèbes et al. (2019).

Appendix B: MATISSE observables

Figure B.1 displays the calibrated squared visibilities and closure phases we used for the image reconstruction.

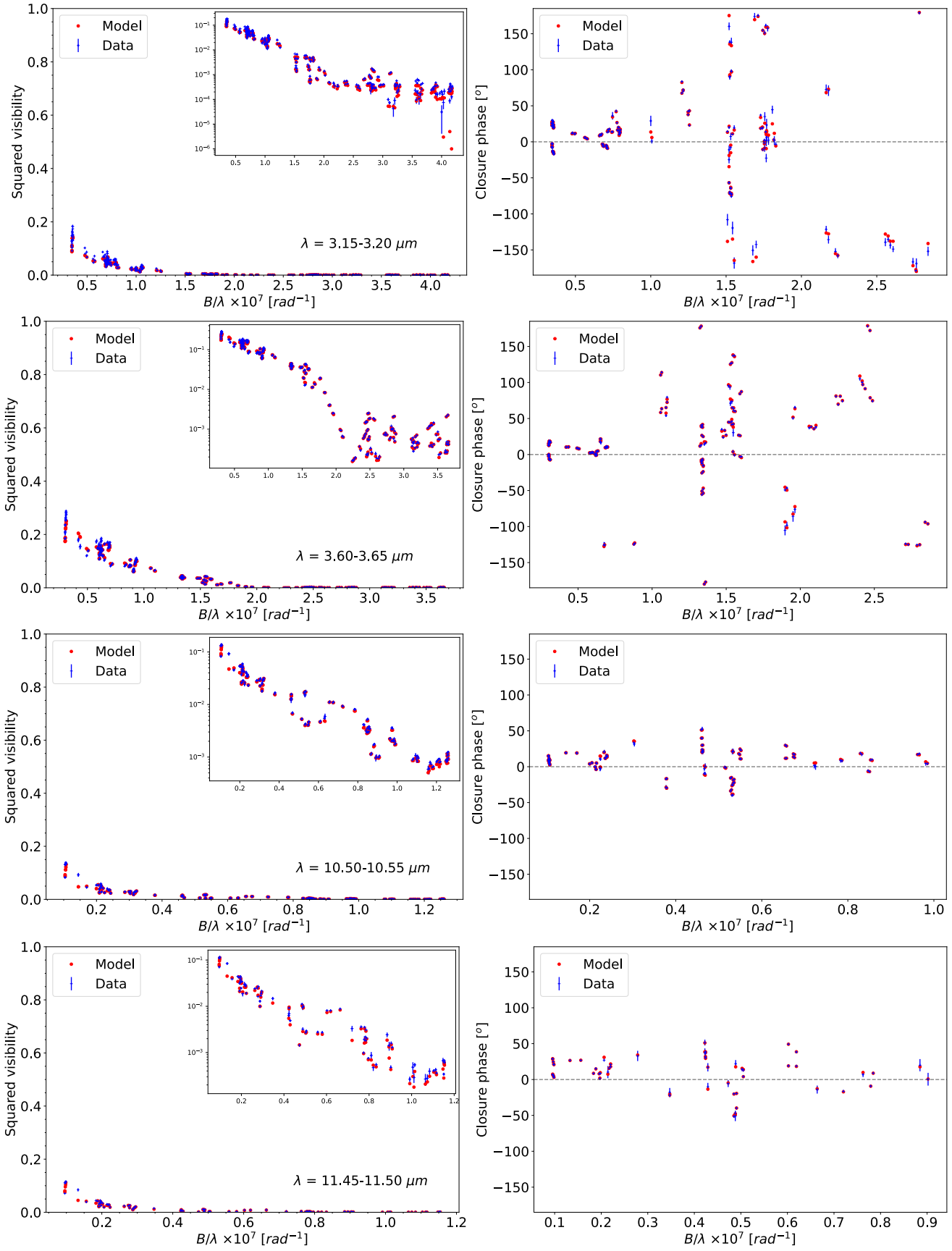

Fig. B.1: Squared visibilities and closure phases from the MATISSE observation (blue error bars). For comparison, the synthetic data from the SQUEEZE image reconstruction are also shown (red dots). The closure phase x-axis represents the longest baseline of each telescope triplet.

Appendix C: Image-reconstruction comparison

Figure C.1 displays the mean SQUEEZE images over the chains, together with images obtained at ±1 standard deviation from the mean. The S/N threshold is defined as the ratio of the mean image over the standard deviation image. The evolution of the posterior distribution for each chain of the four SQUEEZE images is shown in Fig. C.2. Figures C.3 and C.4 compare the images obtained with three image-reconstruction packages. The SQUEEZE procedure is described in Sect. 4, and the packages MIRA and IRBis and their application are described below. To allow a direct comparison of the images, the field of view, the pixel resolution and the spectral range are the same for all three methods.

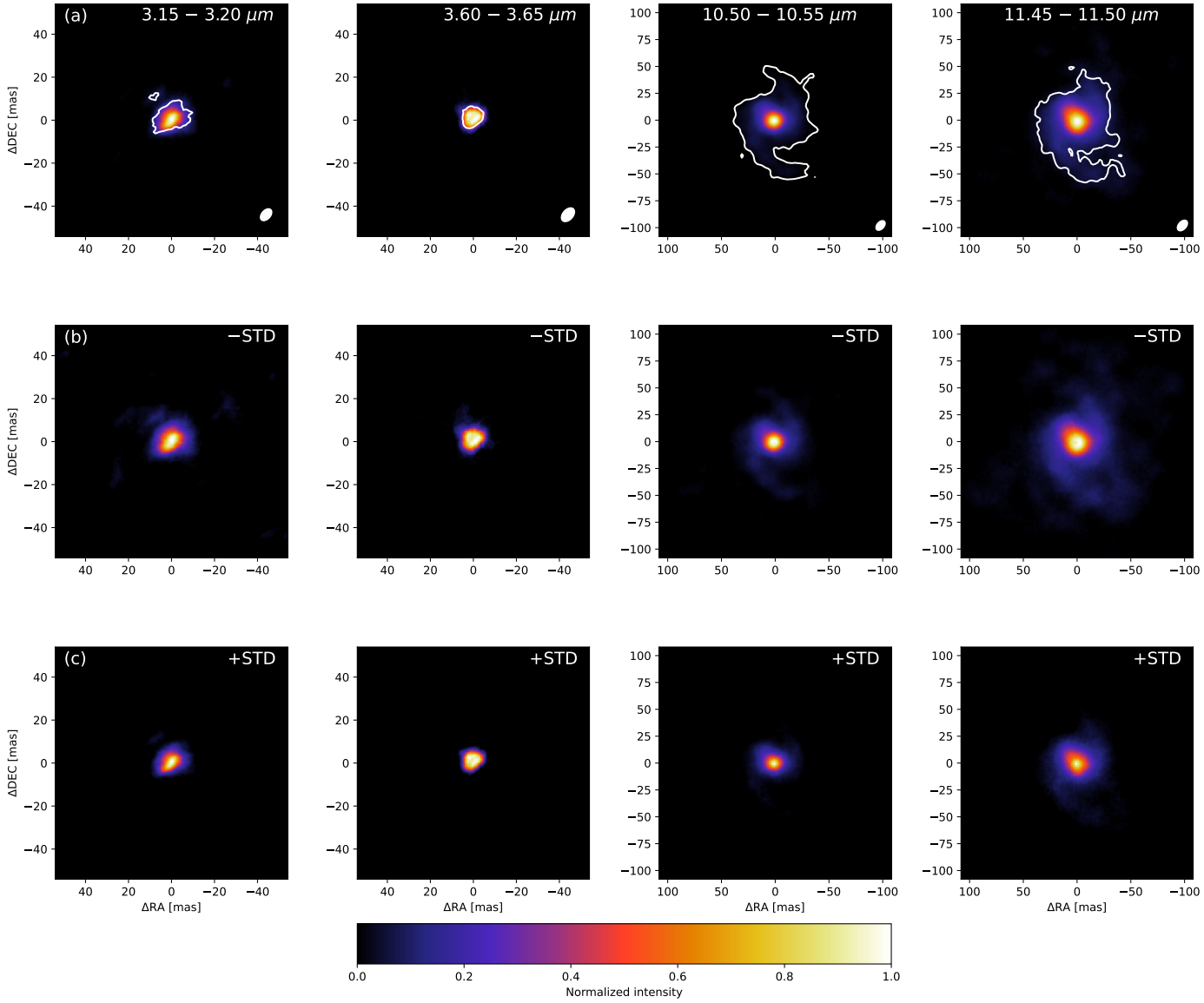

Fig. C.1: SQUEEZE-reconstructed images. (a) Mean image over the chains, (b) image one standard deviation below the mean image, and (c) image one standard deviation above the mean image. The ellipse in the bottom right corner represents the primary synthesised beam. In the upper panels, the white contours are drawn at the 3σ level, defined as three times the S/N threshold.

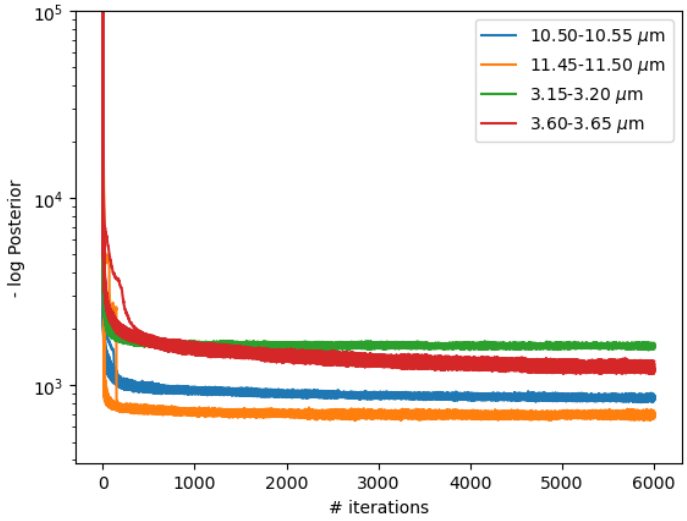

Fig. C.2: Evolution of the posterior distribution as a function of the iteration for the four SQUEEZE images.

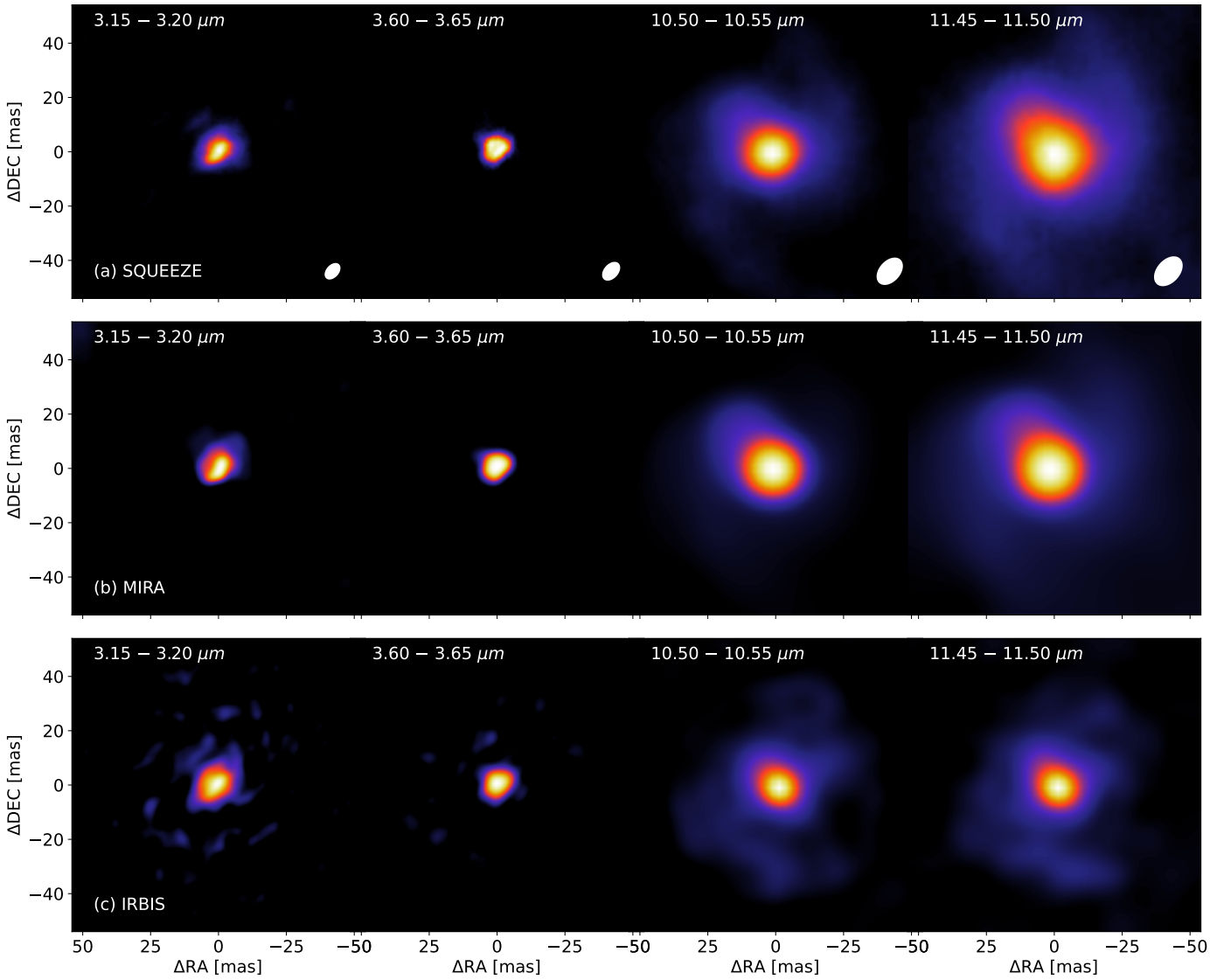

Fig. C.3: Image-reconstruction comparison. From top to bottom: image reconstructed with SQUEEZE (top row), with MIRA (middle row) and with IRBIS (bottom row) for four different wavelength ranges. The images are convolved by a Gaussian beam with an FHWM equal to the angular resolution of the interferometer (from left to right: 2.3 mas, 2.67 mas, 7.75 mas, and 8.45 mas). The colour scale is the same as in Fig. C.1.

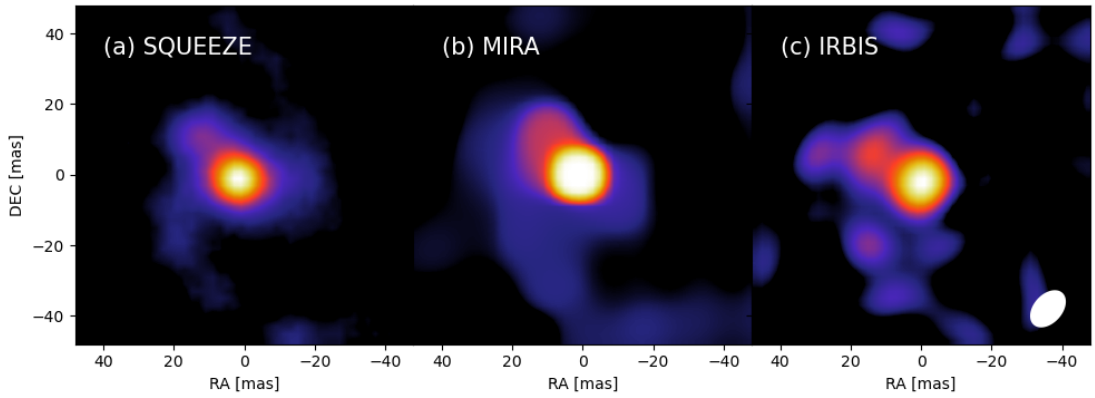

Fig. C.4: Same as Fig. C.3 but for the image reconstructed in the wavelength range 10.50–11.50 μm.

– MIRA procedure: The multi-aperture Image Reconstruction Algorithm (MIRA; Thiébaut 2008) follows a gradient-based search to minimise the weighted sum of the likelihood and a regularisation term that priorities information imposed by the regularizer. The total variation regularization was used with a hyper-parameter, μ, of 10000. The μ value was set using the L-curve technique for values ranging from 0.1 to 100,000 in a semi-log scale. The initial image is a centred Dirac peak. The final images were obtained after performing bootstrapping.
– IRBis procedure: The image reconstruction software using the bispectrum (IRBis; Hofmann et al. 2014) was designed for MATISSE and is included in the mat_tools pipeline. It also uses a gradient-based search but includes additional parameters such as two minimisation engines, six regularisation functions, a weighting of the (u, v)-plane and three cost functions; see Hofmann et al. (2014) for more details. All images were obtained using the cost function 1 (equal weighting of the visibilities and the closure phases in the computation of the χ^2) and the reduction engine 2 (L-BFGS-B). Table C.1 summarises the input parameters used for each image and the χ^2 obtained, for the squared visibility and the closure phase.

Table C.1: IRBis image parameters.

λ [μm]	(u, v)-plane weight	Reg. Func.	μ	$(\chi^2_{V^2}, \chi^2_{CP})$
3.15–3.20	0.5	5	0.05	[0.9, 1.4]
3.60–3.65	0.5	5	0.05	[0.7, 1.6]
10.50–10.55	0.2	6	100	[1.7, 2.9]
11.45–11.50	0.2	2	100	[1.7, 3.4]

Appendix D: Image simulation

D.1: Estimate of the image noise level

To quantify the reliability threshold of the images obtained with SQUEEZE, an artificial model was created and an analogous reconstruction was performed. The artificial model consisted of the median image over the 50 chains obtained for the 11.45 μm range. The interferometric observables (squared visibilities and closure phases) of the artificial image were created using the same (u, v)-coverage. The observables are extracted using the OIFITS modeler (`https://amhra.oca.eu/AMHRA/oifits-modeler/input.htm`) and the same uncertainty values as our observations. The artificial image, its reconstruction and the residual map are displayed in Fig. D.1.

D.2: Dirty beam

The reconstruction artefacts are features without any observational counterparts that arise in the inverse problem due to the limited (u, v)-plane coverage. The best way to identify them is to compute the so-called dirty beam. The dirty beam is computed by taking the Fourier transform of the (u, v)-plane function. The (u, v)-plane function was estimated as Dirac peaks at the spatial frequencies of the interferometric measurements. The dirty beam for the L- and N- band images is shown in Fig. D.2. The shape is the same for both bands but the dimensions of the feature are different as different spatial frequencies are probed. The secondary lobes of the dirty beam have a symmetric spiral shape, with a counter-clockwise winding.

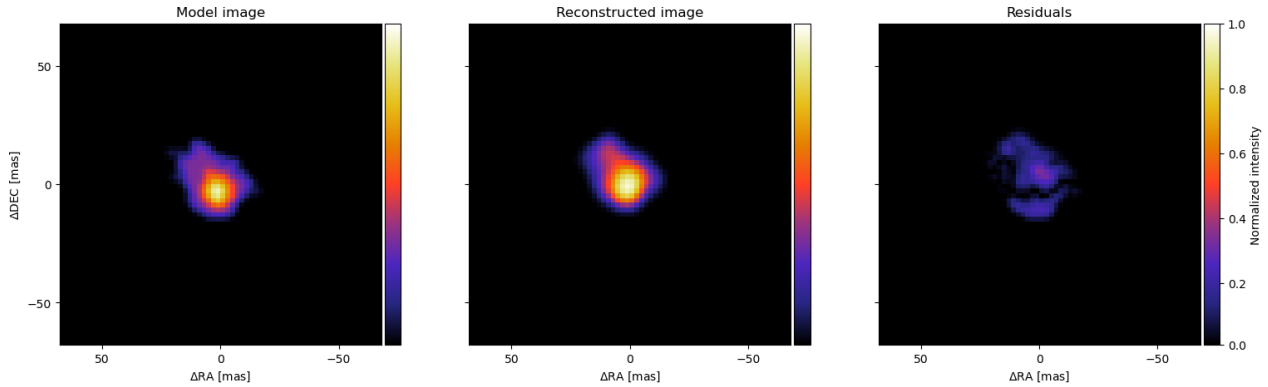

Fig. D.1: Estimate of the image noise level. Left: model image used to assess the reconstruction process. Centre: image reconstructed with the SQUEEZE reconstruction for the 11.45 µm range. Right: residual map. The root mean square of the map is 3.06% of the peak flux level of the original image. This sets the 3σ S/N threshold at 9.2 % in the reconstructed image.

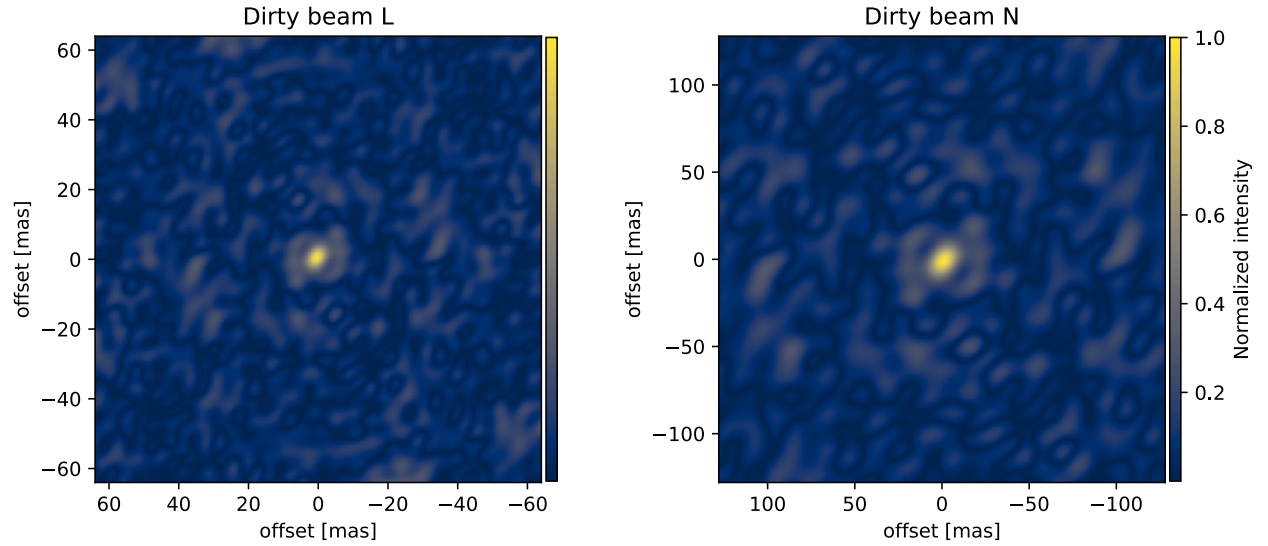

Fig. D.2: Dirty beam estimated for the MATISSE (u, v)-coverage in the L and N bands.

D.3: Estimate of image artefacts

To characterise how the dirty beam impacts the shape of the features obtained, an image error-estimate step was performed. First, the interferometric observables of the mirror image were simulated for the two infrared bands. The mirror image is defined as the final reconstructed image (from Fig. 4), but flipped with respect to the vertical axis. The interferometric observables were extracted from the mirror images using the same (u, v)-plane coverage and similar values for the uncertainties as for the original observables. The images were reconstructed using SQUEEZE and following the same procedure as described in Sect. 4: Fifty simulated-annealing chains, starting with a different 128×128-pixel random image, were run using the transpectral regulariser for 6000 iterations. The final image was obtained by taking the mean image over the chains. Comparison of both images allows us to identify features arising from the dirty beam.

The mirror images and their reconstructed counterparts are displayed in Fig. D.3 for the L band and in Fig. D.4 for the N band. Figure D.3 shows that the L-band mirror image is fully recovered, meaning that the elongated shape is reliable. For Fig. D.4, the mirror image recovered the expected flipped elongation but the background emission displaying a clockwise spiral in the initial image is not recovered. We can therefore conclude that the shape of the spiral feature is not reliable and arises from the reconstruction process.

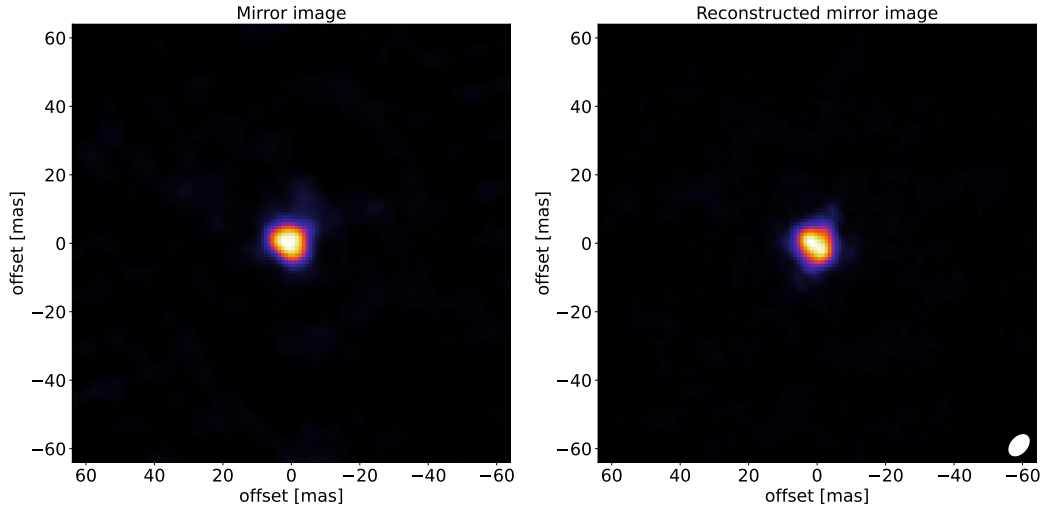

Fig. D.3: Image simulation in the *L* band. Left: simulated mirror image. Right: image reconstructed with SQUEEZE. North is up, and east is left.

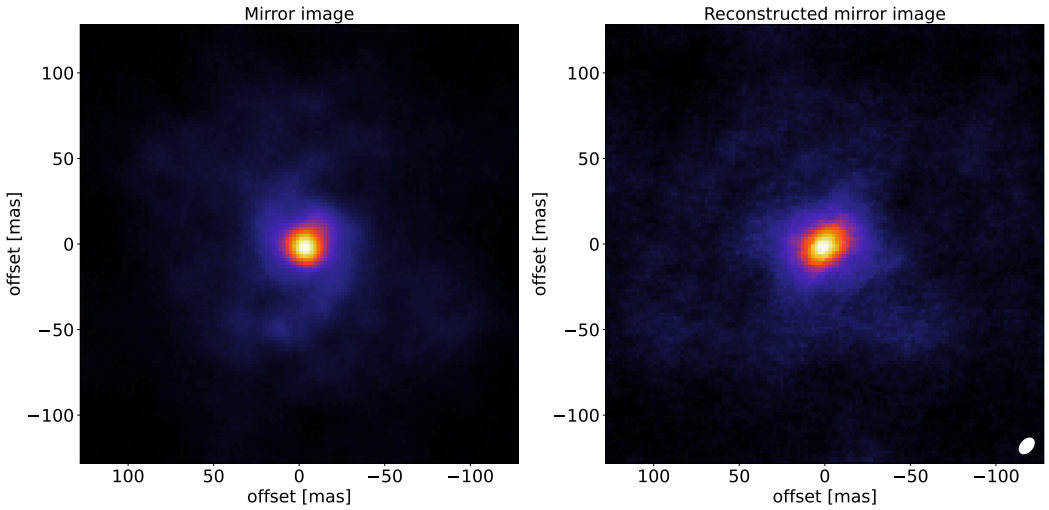

Fig. D.4: Image simulation in the *N*-band. Left: the simulated mirror image. Right: the image reconstructed with SQUEEZE. North is up, East is left.

Appendix E: Photometric data

Table E.1 reports the photometric data (filter name and flux value) used to plot the spectral energy distribution. The data are taken from `https://vizier.cfa.harvard.edu/viz-bin/VizieR` with a search radius of 5″. The WISE photometric fluxes from Schlafly et al. (2020) were disregarded due to their quality factor of 0, implying a heavily saturated detection.

Table E.1: Photometric data used in the spectral energy distribution of V Hya.

Filter	MJD	Flux [Jy]
Tycho:VT	–	2.26 ±0.03
Gaia DR2:Gbp	57204	1.3 ±0.12
Gaia DR2:G	57204	6.84 ±0.32
Gaia DR2:Grp	57204	27.6 ±1.5
Gaia DR3:Gbp	57388	1.7 ±0.07
Gaia DR3:G	57388	13.8 ±0.2
Gaia DR3:Grp	57388	32.0 ±1.9
Johnson: V	51242	5.77 ±0.16
Johnson: J	51242	353 ±101
Johnson: H	51242	859 ±161
Johnson: K	51242	1230 ± 250
2MASS: J	51242	345 ±100
2MASS: H	51242	868 ±162
2MASS: Ks	51242	1270 ± 260
IRAS: 12 μm	–	1110 ±60
IRAS: 25 µm	–	460 ±23
IRAS: 60 µm	–	98.9 ±13.8
IRAS: 100 µm	–	29.9± 4.8
AKARI:N60	–	34.3 ± 12.0
AKARI:WIDE-S	–	54.0 ± 16.2
AKARI:WIDE-L	–	15.2 ± 9.1
AKARI:N160	–	5.1 ± 3.1

Appendix F: VISIR images

Figure F.1 shows the final VISIR coronagraphic image, PSF subtracted, for three percentages of retained frames.

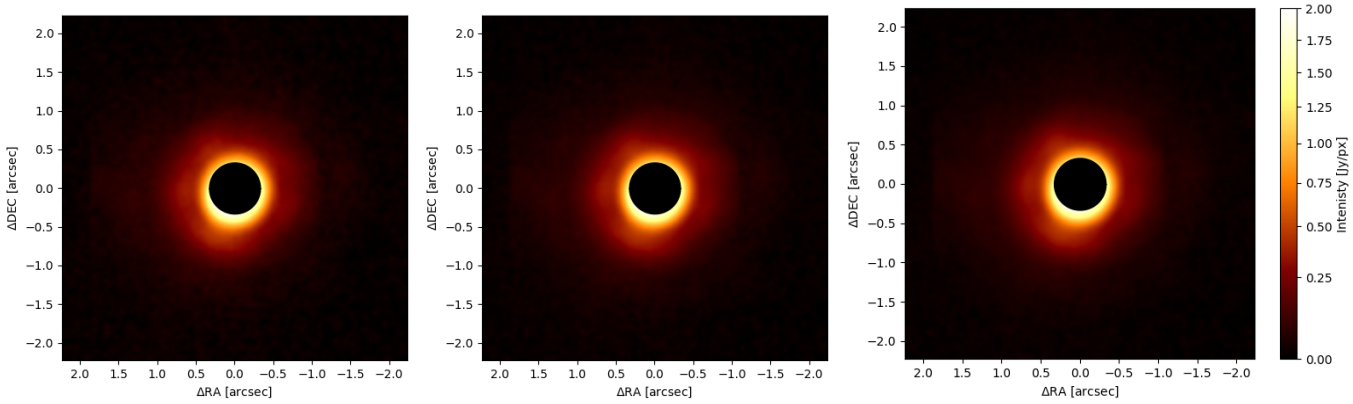

Fig. F.1: VISIR coronagraphic images for rejection yields of 30% (left), 60 % (centre) and 90% (right).